

# 1 A revised mineral dust emission scheme in GEOS-Chem: 2 improvements in dust simulations over China

3 Rong Tian<sup>1</sup>, Xiaoyan Ma<sup>1\*</sup>, Jianqi Zhao<sup>1</sup>

4 <sup>1</sup>Collaborative Innovation Center on Forecast and Evaluation of Meteorological Disasters (CIC-FEMD)/Key Laboratory  
5 for Aerosol-Cloud-Precipitation of China Meteorological Administration, Nanjing University of Information Science &  
6 Technology, Nanjing 210044, China

7  
8 *Correspondence to:* Xiaoyan Ma (xma@nuist.edu.cn)

## 9 10 **Abstract:**

11 Mineral dust plays a significant role in climate change and air quality, but large uncertainties remain in terms of dust  
12 emission prediction. In this study, we improved the treatments of dust emission process in a Global 3-D Chemical Transport  
13 model (GEOS-Chem) v12.6.0, by incorporating the geographical variation of aerodynamic roughness length ( $Z_0$ ), smooth  
14 roughness length ( $Z_{0s}$ ), soil texture, introducing Owen effect and Lu and Shao (1999) formulation of sandblasting efficiency  
15  $\alpha$ . To investigate the impact of the modifications incorporated in the model, several sensitivity simulations were performed  
16 for a severe dust storm during March 27, 2015 to April 2, 2015 over northern China. Results show that simulated threshold  
17 friction velocity is very sensitive to the updated  $Z_0$  and  $Z_{0s}$  field, with the relative difference ranging from 10% to 60%  
18 compared to the original model with uniform value. An inclusion of Owen effect leads to an increase in surface friction  
19 velocity, which mainly occurs in the arid and semi-arid regions of northwest China. The substitution of fixed value of  $\alpha$   
20 assumed in original scheme with one varying with friction velocity and soil texture based on observations reduces  $\alpha$  by 50%  
21 on average, especially over regions with sand texture. Comparisons of sensitivity simulations and measurements show that  
22 the revised scheme with the implement of updates provides more realistic threshold friction velocities and  $PM_{10}$  mass  
23 concentrations. The performance of the improved model has been evaluated against surface  $PM_{10}$  observations as well as  
24 MODIS aerosol optical depth (AOD) values, showing that the spatial and temporal variation of mineral dust are better  
25 captured by the revised scheme. Due to the inclusion of the improvement, average  $PM_{10}$  concentrations at observational  
26 sites are more comparable to the observations, and the average mean bias (MB) and normalized mean bias (NMB) values  
27 are reduced from  $-196.29\mu g m^{-3}$  and  $-52.79\%$  to  $-47.72\mu g m^{-3}$  and  $-22.46\%$  respectively. Our study suggests that the  
28 erodibility factor, sandblasting efficiency and soil-related properties which are simply assumed in the empirical scheme  
29 may lack physical mechanism and spatial-temporal representative. Further study and measurements should be conducted  
30 to obtain more realistic and detailed map of these parameters in order to improve dust representation in the model.

## 31 **1 Introduction**

32 Mineral dust is typically produced by wind erosion from regions with arid and semi-arid surfaces in the world and  
33 exerts significant impacts on the atmospheric radiation balance (Tegen et al., 1996; DeMott et al., 2010; Kumar et al., 2014;  
34 Saidou Chaibou et al., 2020a), climate (DeMott et al., 2003; Mahowald and Kiehl, 2003; Zhao et al., 2012; Chen et al.,  
35 2014; Chin et al., 2014), air quality (Giannadaki et al., 2014; Tian et al., 2019) and human health (Goudie, 2014; Tong et  
36 al., 2017). Dust emission process has been recognized as a leading contributor to dust aerosol loading. Global mineral dust  
37 particles are mainly emitted from North Africa, the Arabian Peninsula, Central Asia, East Asia, Australia and North

38 America, with East Asia (including the Gobi and Taklimakan deserts) accounting for ~20% of the global dust emission  
39 (Ginoux et al., 2004; Nagashima et al., 2016).

40 In order to properly reproduce dust emission process, many dust emission schemes have been developed and  
41 implemented in both global and regional chemical transport models (CTMs) (e.g., Marticorena and Bergametti, 1995; Lu  
42 and Shao, 1999; Alfaro and Gomes, 2001; Shao, 2001, 2004; Shao et al., 2011; Zender et al., 2003; Kok, 2011a, 2011b).  
43 Nevertheless, some intercomparison studies demonstrated that there are large discrepancies among different dust emission  
44 models (Uno et al., 2006; Todd et al., 2008; Huneus et al., 2011; Su and Fung, 2015; Ridley et al., 2016; Chen et al., 2017;  
45 Chen et al., 2019; Ma et al., 2019; Wu et al., 2019; Saidou Chaibou et al., 2020b; Zhao et al., 2020). Ma et al. (2019)  
46 quantitatively evaluated the performance of three dust schemes in WRF-Chem, two schemes in both CHIMERE and  
47 CMAQ, and one scheme in CAMx during a dust episode over northern China. Large differences between observed surface  
48 PM<sub>10</sub> concentrations and modelling results of each model were found. Among schemes in WRF-Chem, AFWA and  
49 UOC\_Shao2004 are better correlated with observations compared to GOCART but tend to overestimate dust  
50 concentrations. Kang et al. (2011) compared the performance of three dust emission schemes in WRF-Chem over East  
51 Asia, showing that the difference of dust emission fluxes between three schemes ranges from an order of 10<sup>1</sup> to 10<sup>2</sup>. Ridley  
52 et al. (2016) showed that the estimated global dust AOD vary by over a factor of 5 among four global models (including  
53 GEOS-Chem, WRF-Chem, CESM and MERRAero), and dust emissions across North Africa are overestimated while  
54 emissions from Asia and the Middle East are underestimated overall. An intercomparison of 14 CTMs as part of the Model  
55 Inter-Comparison Study for Asia (MICS-Asia) phase III project (Chen et al., 2019) showed that nearly all participant  
56 models underestimate PM<sub>10</sub> levels and current CTMs have difficulty producing similar dust emissions when adopting  
57 different dust schemes.

58 The uncertainties in dust emission models can be attributed to a number of issues, such as threshold friction velocity,  
59 surface wind speed, soil texture, particle size distribution, other soil/surface parameters (e.g., soil moisture, vegetation  
60 cover, aerodynamic roughness length) and different physical mechanisms (Tegen, 2003; Zhao et al., 2013; Liu et al., 2018;  
61 Chen et al., 2019). Darменова et al. (2009) conducted a detailed comparison between two schemes developed by  
62 Marticorena and Bergametti (1995) and Shao et al. (1996), indicating that wind friction velocity is a significant factor in  
63 simulating dust emission while the aerodynamic roughness length as well as vegetation cover may play an important role  
64 at higher wind speed. Many sensitivity experiments have been conducted and shown that the modeled threshold friction  
65 velocity can be modified by soil moisture (Cheng et al., 2008; Mokhtari et al., 2012; Gherboudj et al., 2015; Ju et al., 2018),  
66 soil texture (Menut et al., 2013; Gherboudj et al., 2015; Perlwitz et al., 2015a, 2015b; Kontos et al., 2018) and surface  
67 roughness (Cheng et al., 2008; Astitha et al., 2012; Menut et al., 2013), which in turn affects the predicted dust emission.  
68 In addition, a more accurate value of sandblasting mass efficiency ( $\alpha$ ) has been reported to be a crucial factor for a better  
69 performance of dust emission flux (Mokhtari et al., 2012; Klingmüller et al., 2018; Kontos et al., 2018; Ma et al., 2019).

70 Based on the above studies, it is necessary to take these key parameters, including soil-related properties and empirical  
71 input parameters, into fully consideration in a dust emission parameterization. Unfortunately, due to limited observations,  
72 many of these parameters are not well included in the model. For example, most dust models simply assume a constant  
73 values of aerodynamic roughness length and soil clay fraction (Ginoux et al., 2001; Tegen et al., 2002; Zender et al., 2003),  
74 ignoring the temporal and spatial variability of them, which may cause uncertainties to the estimated surface friction  
75 velocity and threshold friction velocity. During recent decades, with the development of observation technology, the  
76 detailed information on the surface characteristics appropriate for global and regional models have been provided (Laurent  
77 et al., 2005, 2008; Prigent et al., 2005, 2012; Shangguan et al., 2014; Perlwitz et al., 2015a, 2015b). Therefore, adopting  
78 more accurate and detailed soil datasets is expected to improve the dust model performance.

79 In this study, we present an improvement of the dust emission scheme in GEOS-Chem model by incorporating the  
80 updated soil texture and aerodynamic roughness length with spatial variability, Owen effect, drag partition correction factor  
81 as well as the updated formulation of sandblasting efficiency, which together significantly improve the prediction of dust

82 emission flux and concentrations over China. The objective is to obtain more realistic surface friction velocity ( $u_*$ ) and  
83 threshold friction velocity ( $u_{*t}$ ) by considering the effect of the soil moisture, surface roughness and soil texture, thus  
84 improving the representation of dust emission in the model.

85 Section 2 gives a detailed description of GEOS-Chem model and the modifications of the improved scheme as well  
86 as numerical experiments and data description. Sensitivity results are compared in Section 3.1 to examine the impacts of  
87 the modifications. Section 3.2 presents the comparisons of the improved scheme and original version with observations, to  
88 evaluate the performance of the improved scheme. Uncertainties, limitations, and future improvements of the emission  
89 scheme are discussed in Section 3.3, followed by a summary in Section 4.

## 90 2 Model and measurements

### 91 2.1 Model description

92 The GEOS-Chem model is a global three-dimensional chemical transport model driven by assimilated meteorology.  
93 In this work, we use ~~a nested version v12.6.0~~ of GEOS-Chem (v12.6.0) driven by GEOS-FP assimilated meteorological  
94 field with a spatial resolution of  $0.25^\circ \times 0.3125^\circ$  and 72 vertical levels for China region ( $15\text{--}55^\circ\text{N}$ ,  $70\text{--}140^\circ\text{E}$ ) during the  
95 period of March 27, 2015 to April 2, 2015. The nested-grid GEOS-Chem is developed by Wang et al. (2004) with lateral  
96 boundary conditions provided by a global simulation (at  $2^\circ \times 2.5^\circ$  resolution in this study). The lateral boundary conditions  
97 is provided by a global simulation of  $2^\circ \times 2.5^\circ$ . Many nested-grid GEOS-Chem simulations have been evaluated and  
98 applied to the analysis of gaseous and aerosol species over China (Chen et al., 2009; Lin et al., 2014; Zhang et al., 2015;  
99 Wang et al., 2013; Li et al., 2019).

100 GEOS-Chem includes detailed atmospheric chemical mechanism and online aerosol calculations. In this work, we  
101 simulate the dust emission with a combination of the dust entrainment and deposition (DEAD) mobilization scheme  
102 (Zender et al., 2003) and Global Ozone Chemistry Aerosol Radiation and Transport (GOCART) source function. Mineral  
103 dust aerosols are distributed across 4 size bins (with radius bins of 0.1–1.0, 1.0–1.8, 1.8–3.0, and 3.0–6.0  $\mu\text{m}$ ). The mass  
104 fractions of each size bin are parameterized by the optimized dust particle size distribution proposed by Zhang et al. (2013).  
105 Dry deposition velocities for dust aerosols are computed with the gravitational settling scheme of Fairlie et al. (2007) and  
106 aerosol deposition scheme from Zhang et al. (2001). Wet deposition scheme, which includes scavenging in convective  
107 updrafts, as well as rainout and washout of soluble tracers, is described in Liu et al. (2001). Aerosol optical depth is derived  
108 online from aerosol concentrations with externally-mixed assumption using RH-dependent aerosol optical properties from  
109 Latimer and Martin (2019). Dust optics are from Ridley et al. (2012).

### 110 2.2 Improvement on the dust emission scheme in GEOS-Chem

111 The standard dust emission scheme in GEOS-Chem is based on a semi-empirical formulation developed by Zender et  
112 al. (2003) and is combined with GOCART source function (Ginoux et al., 2001). In this scheme, the vertical dust flux ( $F$ )  
113 is proportional to the horizontal saltation flux ( $Q_s$ ), which is the function of surface friction velocity ( $u_*$ ) and threshold  
114 friction velocity ( $u_{*t}$ ):

$$115 \quad F = (1 - A_s)S\alpha Q_s \quad (1)$$

$$116 \quad Q_s = C_z \frac{\rho_{air}}{g} u_*^3 \left(1 - \frac{u_{*t}}{u_*}\right) \left(1 + \frac{u_{*t}}{u_*}\right)^2 \quad u_* > u_{*t} \quad (2)$$

117 where  $\alpha$  is the vertical-to-horizontal flux ratio or sandblasting efficiency, based on the soil clay content (Marticorena and  
118 Bergametti, 1995).  $S$  is based on GOCART source function (see Fig. S1), also named as the soil erodibility factor,  
119 representing the grid cell fraction of the bare land suitable for mobilization.  $A_s$  is the fraction of snow-covered surface.  $C_z$   
120 is the saltation constant ( $C_z=2.61$ ).

121 According to the equation,  $u_{*t}$ ,  $u_*$  as well as  $\alpha$  are the key input parameters in the accurate prediction of dust

122 emission flux.  $u_{*t}$  is used to describe the characteristics of soil and land surface condition, representing the resistance of  
 123 surface to wind erosion. In the standard dust scheme,  $u_{*t}$  is calculated using a semi-empirical formulation as a function  
 124 of air density and soil particle density (Iversen and White, 1982). Furthermore, two correction terms, including soil  
 125 moisture correction (Fécan et al., 1999) and drag partition correction (Marticorena and Bergametti, 1995), are also applied  
 126 to modify  $u_{*t}$ . It should be noted that in the original scheme, the drag partition correction term is eliminated.

127  $u_*$  is a description of surface wind speed, which mainly depends on 10m wind speed taken from meteorological field  
 128 assuming neutral stability (Bonan, 1996). Owen effect, which represents a positive feedback between saltation process and  
 129 friction speed (Owen, 1964), is often adopted in models to modify  $u_*$ . However, Owen effect is eliminated in the original  
 130 scheme.

131 Sandblasting efficiency  $\alpha$  is parameterized according to the empirical relation described by Marticorena and  
 132 Bergametti (1995) (MB95), which depends on the soil clay content ( $M_{clay}$ ) and is restricted to  $M_{clay} < 20\%$ :

$$133 \quad \alpha = 100e^{(134M_{clay}-6)\ln 10} \quad (3)$$

134 However, in the global model,  $\alpha$  tends to be overly sensitive to  $M_{clay}$ . Due to this reason, a globally fixed value of  
 135  $M_{clay} = 20\%$  is assumed in current model (Zender et al., 2003).

136 It should be noted that, some input parameters, data or formulations are quite simplified and need to be improved  
 137 based on the original dust scheme described above. For example, the aerodynamic roughness length ( $Z_0$ ), the smooth  
 138 roughness length ( $Z_{0s}$ ) as well as the mass fraction of clay in the soil ( $M_{clay}$ ) are assumed as a constant uniformly, despite  
 139 the fact that it may vary with time and location. As a result, the simulation of related processes, such as drag partition effect  
 140 or soil moisture effect, may lack spatial representation. Therefore further modifications on these variables should be made  
 141 in order to obtain more realistic dust emission. Fig. S2-1 presents the schematic diagram of the dust emission schemes in  
 142 the standard model and the modifications incorporated in this study. The details of the parameterization options and  
 143 required input parameters are presented in following sections.

### 144 2.2.1 Soil Type and Soil Texture Data

145 In the model,  $M_{clay}$  can have an impact on  $u_{*t}$  through modifying soil moisture correction term, thus influencing the  
 146 modeled dust emission flux. The soil moisture correction term, defined as  $f_w$ , is parameterized according to Fécan et al.  
 147 (1999), which accounts for the increase of  $u_{*t}$  with soil moisture content.

$$148 \quad f_w = \begin{cases} 1 & w < w' \\ [1 + 1.21(w - w')^{0.68}] & w \geq w' \end{cases} \quad (4)$$

$$149 \quad w'(\%) = a(0.0014M_{clay}^2 + 0.17M_{clay}) \quad (5)$$

150 where  $w$  is gravimetric soil moisture and  $w'$  is soil residual moisture.

151 With the increase of soil moisture, soil cohesion can be enhanced, particularly over regions with high clay content,  
 152 thus inhibiting sandblasting process to some extent. However, as stated above,  $M_{clay}$  is assumed as a constant equal to 20%  
 153 in the original scheme, which can cause uncertainty in dust prediction. In the improved scheme, we employ the gridded  
 154 data of clay content from the Global Soil Dataset for use in Earth System Models (GSDE) (Shangguan et al., 2014), which  
 155 is based on the Soil Map of the World and various regional and national soil databases. Fig. 4-2 shows the updated  $M_{clay}$   
 156 from Shangguan et al. (2014) with the horizontal resolution of  $2^\circ \times 2.5^\circ$  at the global scale. Compared to the original fixed  
 157 value of 20%, the updated  $M_{clay}$  is generally lower in most of the dust source areas over East Asia.

### 158 2.2.2 Surface roughness length

159 The drag partition is used to describe the impact of roughness elements (such as rocks, pebbles, vegetation, etc.) on  
 160  $u_{*t}$ . According to Marticorena and Bergametti (1995), the roughness correction term,  $f_d$ , is a function of the aerodynamic  
 161 roughness length  $Z_0$  and the smooth roughness length ( $Z_{0s}$ ):

$$f_d = 1 - \frac{\ln\left(\frac{Z_0}{Z_{0s}}\right)}{\ln\left[0.7\left(\frac{12255\text{cm}}{Z_{0s}}\right)^{0.8}\right]} \quad (6)$$

where the required roughness lengths are set as the constant values of  $Z_0 = 0.01$  cm and  $Z_{0s} = 0.0033$  cm globally.

$Z_0$  represents the roughness length of the overlying non-erodible elements (solid obstacles, such as rocks), which transfers part of the wind momentum from the atmosphere to the surface, dissipating the shear force for particle saltation. Prigent et al. (2005) derived global aerodynamic roughness length in arid and semi-arid areas which are retrieved from the ERS-1 satellite measurements with a horizontal resolution of  $0.25^\circ \times 0.25^\circ$ . Here we apply the global monthly mean  $Z_0$  fields provided by Prigent et al. (2005) and then re-grid the map to  $2^\circ \times 2.5^\circ$  horizontal resolution for the incorporation into GEOS-Chem. As Fig. 2-3 shows, compared to the fixed constant assumed in the original version, the updated global  $Z_0$  is generally higher. Over northern China, the  $Z_0$  value ranges from approximately 0.01cm over desert regions to 0.07cm.

$Z_{0s}$  characterizes the roughness length of the uncovered, bare erodible surface. Instead of setting  $Z_{0s}$  to a fixed value, some studies suggested that  $Z_{0s}$  can be estimated as 1/30 of the coarse-mode mass median diameter (MMD) of soil particles, which will provide more realistic representation of soil texture distribution (Marticorena and Bergametti, 1995; Laurent et al., 2006; Mokhtari et al., 2012). In the improved version, we adopt this empirical formula, based on updated soil texture classification (Mokhtari et al., 2012; Xi et al., 2015), to estimate  $Z_{0s}$ :

$$z_{0s} = MMD/30 \quad (7)$$

where MMD is the median diameter of the coarsest mode for various soil textures shown in Table 1. The corresponding  $Z_{0s}$  for different soil types are listed in Table 1 and its global distribution is shown in Fig. 34. The soil texture map is obtained based on the Harmonized World Soil Database (HWSD; <http://www.iiasa.ac.at/Research/LUC/External-World-soil-database/HTML>), which provides global sand, silt, and clay contents at 30 arc-second resolution. The soil texture dataset is re-gridded to  $2^\circ \times 2.5^\circ$  resolution, and then is applied to identify the global soil texture by using the United States Department of Agriculture (USDA) soil texture triangle (based on the amount of sand, clay, and silt contents; <http://soils.usda.gov/technical/aids/investigations/texture/>). There are 12 classes of soil defined by USDA. It can be seen from Fig. 4-5 that loam, sandy loam and clay loam, are the dominant soil types over China. Among them, sandy loam and loam occupy the major part of northwest China.

### 2.2.3 Sandblasting efficiency $\alpha$

Sandblasting efficiency  $\alpha$  is important in the dust emission calculation as it is used to convert the horizontal saltation mass flux to a vertical dust mass flux. In the original scheme,  $\alpha$  is simply expressed as a function of  $M_{\text{clay}}$ , which is a fixed value of 20%. The assumption in the original scheme might cause uncertainty in modeled flux and make the spatial variation less representative (Mokhtari et al., 2012).

In order to reduce this uncertainty, a more physically-based function from Lu and Shao (1999) (LS99) is adopted in our study. Based on wind tunnel experiments carried out by Rice et al. (1996a, b), Lu and Shao (1999) derived the expression of  $\alpha$  through theoretical calculation and some simplifications:

$$\alpha = \frac{C_\alpha g f \rho_b}{2p} (0.24 + C_\beta u_* \sqrt{\frac{\rho_p}{p}}) \quad (8)$$

where  $f$  is the fine particles content in the soil volume,  $p$  is soil plastic pressure, which represents the magnitude of the surface resistance ( $\text{N m}^{-2}$ ),  $\rho_b$  and  $\rho_p$  are the bulk soil density and particle density, respectively,  $g$  is the gravitational acceleration ( $\text{m s}^{-2}$ ),  $u_*$  is friction velocity ( $\text{m s}^{-1}$ ), and  $C_\alpha$  and  $C_\beta$  are empirical constants. Among these parameters, the values of  $\rho_b$  and  $p$  depend upon different soil textures. Some studies (Kang et al., 2011; Foroutan et al., 2017; Ma et al., 2019) have implemented this formulation in the model and proposed the proper range of these parameters over different soil types.

Many measurements from laboratory experiments and field observations have demonstrated the close relationship between  $\alpha$  and  $u_*$  (Gillette et al., 1997; Gomes et al., 2003; Rajot et al., 2003; Roney and White, 2006; Macpherson et al.,

204 2008; Panebianco et al., 2016; Zhang et al., 2016). To improve the original scheme, we extract  $\alpha$  from these measurements  
205 over different soil types, based on the expression of LS99, as depicted in Fig. 5-6 and Table 2.

## 206 2.3 Experiments design

207 Several sensitivity experiments (Table 3) are conducted to assess the model performance of the modifications in the  
208 improved scheme. Control is the control run with the dust emission scheme originally implemented by Fairlie et al. (2007).  
209 Sen\_mclay, Sen\_owen, Sen\_ratio, Sen\_drag and Sen\_Z<sub>0</sub>Z<sub>0s</sub> are the same as the control run but including the modification  
210 of M<sub>clay</sub>, Owen effect, sandblasting efficiency, drag partition effect and updated surface roughness length (Z<sub>0</sub> and Z<sub>0s</sub>)  
211 respectively. Sen\_all represents the simulation with the improved scheme which accounts for all the modification described  
212 above.

## 213 2.4 Measurements

214 The data used in this study includes the Moderate Resolution Imaging Spectrometer (MODIS) Level 3 AOD data,  
215 hourly observational data of surface PM<sub>10</sub> concentration, and meteorological field taken from the Meteorological  
216 Information Comprehensive Analysis and Process System (MICAPS). The data used in this study is for the period of March  
217 27, 2015 to April 2, 2015.

218 MODIS aerosol products are used to evaluate model results of AOD. MODIS AOD at 550 nm is obtained from the  
219 daily level-3 product from Aqua satellites (MYD08\_D3, 1°×1° gridded data) and is combined with Deep Blue retrievals  
220 which can provide AOD over bright surfaces (i.e., desert regions).

221 Hourly surface observed PM<sub>10</sub> concentration data, collected from about 1000 environmental monitoring stations  
222 maintained by Chinese Ministry of Environmental Protection (MEP; <http://datacenter.mep.gov.cn>), is used to validate the  
223 model performance of surface dust concentrations.

224 Meteorological fields of wind speed taken from the Meteorological Information Combine Analysis and Process system  
225 (Micaps) developed by the Chinese National Meteorological Center (NMC) are used for evaluation of wind field in the  
226 model. Fig. S3S2-S4-S3 show that the 10m wind field used in the model scheme generally agree well with the Micaps  
227 observations over most sites. However, comparisons of averaged surface wind field between the model input and  
228 observations (Fig. S5S4) show that although the circulation patterns in the model are identical with the observations,  
229 surface wind speed in the model tend to be larger than observations ([which was also found by Wang et al. \(2014\)](#)), especially  
230 over western and northeastern Inner Mongolia.

## 231 3 Results and discussion

### 232 3.1 Sensitivity study

233 In order to assess the sensitivity of the dust emission to the modified input parameters or physical processes, several  
234 numerical experiments are conducted and compared. Fig. 6a-7a presents the relative difference (%) of averaged  $u_{*t}$  during  
235 study period between these sensitivity simulations and the control run. The  $u_{*t}$  simulated by Control run are generally  
236 small, with values less than 0.3m/s (not shown). Wu et al. (2013) indicated that  $u_{*t}$  over source regions in northern China  
237 calculated by Zender et al. (2003) are generally lower (with values ranging from 0.2 to 0.25 m/s) than the measurement  
238 (with values ranging from 0.34 to 0.69 m/s) and the values calculated by Shao (2004), which is closer to the observations.  
239 The sensitivity simulations show that the update of M<sub>clay</sub> in Sen\_mclay can lead to higher  $u_{*t}$  over northern China and  
240 lower  $u_{*t}$  over southern China than the control simulation, which overestimates M<sub>clay</sub> over northern China while  
241 underestimates it over southern China by setting M<sub>clay</sub> to 20%. In northern China, particularly in arid and semi-arid regions,  
242 the updated M<sub>clay</sub> will decrease the soil moisture threshold  $w'$  and increase soil moisture term  $f_w$ , thus leading to a slight

243 increase in  $u_{*t}$  (with magnitude <10%). The inhibition of dust emission by surface roughness elements is not taken into  
244 account in the original scheme, i.e.,  $f_d=1$ . Some studies (Darmenova et al., 2009; Menut et al., 2013) have demonstrated  
245  $f_d$  as a function of  $Z_0$  and  $Z_{0s}$ , implying that  $f_d$  increase with  $Z_0$  and decrease with  $Z_{0s}$ . Compared to the fixed values used  
246 in the original scheme, updated  $Z_0$  field used in Sen\_  $Z_0Z_{0s}$  are generally larger and updated  $Z_{0s}$  field are smaller. Therefore,  
247  $f_d$  are increased significantly, particularly over the regions with non-erodible elements (larger  $Z_0$ ). Result shows that  $u_{*t}$   
248 is increased when considering the drag partition effect (increased by 10% in Sen\_drag with constant  $Z_0$  field), particularly  
249 with the updated  $Z_0$  and  $Z_{0s}$  field (increased by 10%~60% in Sen\_  $Z_0Z_{0s}$ ). In general, due to the inclusion of  $Z_0$ ,  $Z_{0s}$  and  
250  $M_{clay}$ ,  $f_d$  and  $f_w$  are modified, which results in significant alteration in  $u_{*t}$  (ranging from -8%~72% in Sen\_all) over  
251 China. It can be found that the modification of  $f_d$  due to updated  $Z_0$  and  $Z_{0s}$  makes more contribution to the increase in  
252  $u_{*t}$ .

253 Relative difference of  $u_*$  with respect to the control run are also compared in Fig. 6b7b. Considering Owen effect in  
254 Sen\_owen leads to an increase in  $u_*$  by 0%~39%, especially over northwest China where surface wind is strong. Modeled  
255  $u_*$  is obtained from  $u_{10m}$  and  $Z_0$  under neutral conditions (Bonan, 1996). It can be seen that updated  $Z_0$  in Sen\_  $Z_0Z_{0s}$  can  
256 modify  $u_*$  by influencing the boundary-layer exchange properties.  $u_*$  over northern China is generally increased by  
257 10%~22% with higher values of  $Z_0$  in Sen\_  $Z_0Z_{0s}$ , while it is slightly decreased over Taklimakan and Gobi deserts. In  
258 Sen\_all, modeled  $u_*$  is increased by 5%~50% over most parts of China.

259 Fig. 6e-7c presents the percentage difference in terms of sandblasting efficiency  $\alpha$ . In the original version,  $\alpha$  is set as  
260 a uniformly constant value (around 0.04) due to the assumption of a fixed  $M_{clay}$ . In Sen\_ratio and Sen\_all,  $u_*$ -dependent-  
261 ratio following LS99, which varies with different soil texture according to observations, is adopted. On average,  $\alpha$  is  
262 decreased by 50% with the modification in Sen\_ratio and Sen\_all. The largest reduction occur over regions with sand  
263 texture such as over Taklimakan and Gobi Desert.

264 As seen from Fig. 6d7d, the simulated dust emission flux ( $F$ ) vary significantly among different experiments. Due to  
265 the inclusion of updated  $M_{clay}$ , soil moisture term increases in Sen\_mclay, which leads to higher  $u_{*t}$  and lower  $F$  over  
266 most regions. Accounting for Owen effect in Sen\_owen results in an increase in  $F$  of 0%~314%, particularly over northern  
267 part of Gansu Province and northwestern Inner Mongolia. A significant reduction in arid and semi-arid regions of northern  
268 China is caused by updated  $\alpha$  (Sen\_ratio). In Sen\_drag and Sen\_  $Z_0Z_{0s}$ ,  $F$  are influenced by -100% ~-4% and -100%~50%  
269 respectively as a result of the inclusion of  $f_d$  with constant  $Z_0$  and updated  $Z_0$ ,  $Z_{0s}$  respectively. Due to the combined  
270 effects of the modifications,  $F$  simulated by Sen\_all is generally reduced over northern China, except  
271 in some regions of northwest China, where Owen effect plays a dominant role.

272 ~~Five~~ sites closer to dust source area or significantly influenced by dust-storms (~~Beijing, Xilinguole, Huhehaote,~~  
273 ~~Jiuquan, and Kuele and Akesu~~, locations shown in Fig. S1) are selected to evaluate the performance of control and  
274 sensitivity simulations. Comparisons of the modeled  $u_{*t}$  (Fig. 78) show that in all sites, modeled  $u_{*t}$  are increased in  
275 Sen\_mclay, Sen\_drag, Sen\_  $Z_0Z_{0s}$  and Sen\_all, compared with the original model, with the highest  $u_{*t}$  simulated by  
276 Sen\_all. Modeled  $u_{*t}$  increase from 0.2223~0.25m/s in Control to 0.3229~0.37m/s in Sen\_all. The reported  $u_{*t}$  values  
277 over arid and semi-arid regions of China are around 0.3~0.5m/s (Wang et al., 2009). Wu et al. (2013) summarized that  $u_{*t}$   
278 range from 0.34~0.69m/s over East Asia and indicated that  $u_{*t}$  calculated by Zender et al. (2003) are relatively lower,  
279 ranging from 0.2m/s to 0.25m/s. It is apparent that modeled  $u_{*t}$  are greatly increased in the revised simulation, which is  
280 much closer to the observed values. This improvement is mainly attributed to the update of  $Z_0$  and  $Z_{0s}$ . Comparisons  
281 between the modeled averaged  $PM_{10}$  concentrations and the observational values in four sites show that  $PM_{10}$  levels  
282 simulated by Sen\_all are closer to observations than many other cases. In summary, Sen\_all shows the better agreement  
283 with the observations in terms of  $u_{*t}$  and  $PM_{10}$  concentrations.

### 284 3.2 Comparison between the improved scheme and the original scheme with observations

285 In order to validate the model performance of the improved scheme, time series of the observed surface  $PM_{10}$

286 concentrations are compared against the modeled values from Control (the original scheme) and Sen\_all (the improved  
287 version) during a dust episode from 27 March to 2 April of 2015 over northern China. The intensity and evolution of this  
288 dust event has been described by Wang et al. (2017), illustrating that dust particles were mainly emitted from Mongolia  
289 and Inner Mongolia province of China and a dust backflow event took place over North China on March 29. Fig. 8-9  
290 compares the hourly modeled PM<sub>10</sub> concentrations and observed values for nine selected sites (locations shown in Fig.  
291 S4S3), which are closer to the dust sources or severely affected by the dust event. It shows that the dust concentrations are  
292 generally underestimated in Control run, particularly when dust concentrations are quite high, indicating that the original  
293 scheme has difficulty in accurately reproducing the dust emission process. Sen\_all generally reproduce the PM<sub>10</sub> levels  
294 better than Control run. Both the magnitude and the temporal evolution of PM<sub>10</sub> concentrations are captured in Sen\_all  
295 quite well, with peak values much closer to the observations. Among these sites, Sen\_all shows better performance over  
296 North China, e.g., Beijing, Tianjin and Huhehaote. But both Control run and Sen\_all fail to capture the peak values from  
297 29 March to 30 March. During this period, dust particles, mixed with anthropogenic pollutants, flew back due to the south  
298 wind over North China (Wang et al., 2017). Uncertainties in the meteorological field and dust heterogeneous reactions in  
299 the model may cause the model bias.

300 For specific periods, however, modeled peak values of some sites occur earlier (several hours) than the observations  
301 at some sites (e.g., Beijing and Tianjin in 28 March), which could be considered as a result from the uncertainty in the wind  
302 field used in the model. It shows that the surface wind is stronger in the model than the observations (Fig. S3S2), which  
303 may lead to stronger transport of the dust from source regions to downwind areas such as Beijing, Tianjin and Kuele.  
304 Instead, modeled and observed peak values of some sites in the source regions (e.g., Huhehaote, Xilinguole and Hami)  
305 almost simultaneously occur.

306 In order to quantify the performance of the model result, some statistical parameters, including the mean values,  
307 correlation coefficient (R), mean bias (MB), normalized mean bias (NMB), are calculated and listed in this paper. The  
308 statistical performance for the modeled surface PM<sub>10</sub> concentrations from Control run and Sen\_all against observations  
309 are presented in Table 4. It shows that dust concentrations at all selected sites are significantly underestimated in Control  
310 run, especially over northwest regions, with the MB and NMB values ranging from -163.5 $\mu\text{g m}^{-3}$  to -503.61 $\mu\text{g m}^{-3}$  and  
311 -64.61% to -68.48% respectively. It is obvious that Sen\_all with updated modification greatly improves the dust  
312 concentration prediction, with mean values more comparable to the observations, and the average MB and NMB values  
313 reduce from -196.29 $\mu\text{g m}^{-3}$  and -52.79% in Control run to -47.72 $\mu\text{g m}^{-3}$  and -22.46% respectively. The largest  
314 improvement occurs at northwest stations (e.g. Hami, Akesu and Kuele), which are located close to Taklimakan desert.  
315 Over other regions, such as North China (e.g., Beijing, Tianjin, Huhehaote and Xilinguole), the model performance of  
316 Sen\_all are slightly better than Control run.

317 Although the MB and NMB values of most stations are generally lower and the mean values are much closer to  
318 observation for Sen\_all simulation, i.e., modifications included improve the underestimation in Control run to some extent,  
319 the dust concentrations are still generally underestimated. For stations closer to Gobi desert, such as Xilinguole, Jiuquan  
320 and Baiyin, dust concentrations are greatly underestimated with NMB<-30%, which is likely due to the uncertainty in the  
321 erodibility factor over Gobi desert used in our study (Ginoux et al., 2001). Similarly, Su and Fung (2015) evaluated the  
322 performance of dust emission schemes in WRF-Chem over East Asia, pointing out that the erodibility factor from Ginoux  
323 et al. (2001) over the Gobi desert is significantly underestimated, which may result in the underestimation of the dust  
324 emission over the Gobi desert. Given that simulated dust emission flux is directly scaled by erodibility factor, we suggest  
325 that the erodibility factor used in our model needs to be updated or improved.

326 As stated above, although the model can capture the overall temporal variations of surface dust concentrations, the  
327 occurrence of modeled peak values show earlier (about six hours) than the observations over several stations, which may  
328 be attributed to strong transport due to stronger surface wind used in the model. It should be noted here that this model bias  
329 contributes a lot to the simulation error, leading to smaller R and greater MB, NMB values. R values will be greatly



330 improved if this bias is eliminated, implying that the input assimilated meteorological field is important for dust emission  
331 simulation and needs to be further evaluated and adjusted.

332 The averaged modeled surface  $PM_{10}$  concentrations with and without the modifications (Sen\_all and Control run  
333 respectively) and observational values at ~1400 stations over China during the study period are compared in Fig. 910. It  
334 shows that dust concentrations are generally underestimated in Control run (NMB=-16%, regression slope=0.4), which  
335 could be attributed to the crude representation of soil properties, roughness length and other related elements. Incorporating  
336 improvements in scheme makes the modeling result much closer to the observations, with R values increasing from 0.6 to  
337 0.7, NMB values changing from -16% to -11%, regression slope ranging from 0.4 to 0.6. However, the improved model  
338 still tends to underestimate the dust concentrations. Unrealistic soil properties (e.g., soil texture; roughness length) and  
339 insufficiently accurate potential source map (the erodibility factor) used to scale dust emission flux could be the possible  
340 causes.

341 To further investigate the model performance, spatial distributions of averaged simulated surface  $PM_{10}$  concentrations  
342 from Control run and Sen\_all and their comparisons against observations are presented in Fig. 1011. Results show that  
343 both Control run and Sen\_all can reproduce the pattern of dust concentrations in the study region, with high values located  
344 over northwest China, North China and some areas of northeast China, indicating that GEOS-Chem can represent the main  
345 features of dust emission and transport during the dust storm. It is found that for most sites in Control run, the simulated  
346 magnitude are close to the observational values, but are underestimated over northwest China (where Gobi and Taklimakan  
347 deserts are located) and North China plain. The simulated values from Sen\_all are generally larger than Control run, and  
348 are more consistent with measurements both in magnitude and in area extent, especially  
349 over the desert region of northwest China. However, dust concentrations are still underestimated over North China plain,  
350 possibly due to outdated source map or some potential dust source regions over Inner Mongolia are not well included. In  
351 addition, missing mechanism of secondary aerosol source in the model such as heterogeneous reactions could also cause  
352 the model bias (Zheng et al., 2015; Cheng et al., 2016).

353 Figure- 11-12 shows the spatial distribution of simulated averaged AOD from Control run and Sen\_all as well as  
354 MODIS AOD for the study period. For better comparison, simulated AOD at 13:00 local time (Aqua passage time) are  
355 extracted. Result shows that Control run reproduces the major regions with high AOD values, e.g., eastern China, but with  
356 lower magnitude. Control run also fails to capture the high-AOD area over the Taklimakan desert, while Sen\_all could  
357 capture it. Compared with Control run, Sen\_all generally reproduce the spatial coverage and magnitude of the observed  
358 AOD.

### 359 3.3 Discussion

360 In our study, we point out that the erodibility factor (S) in the model may introduce uncertainty in modeled dust  
361 concentrations, especially over Gobi desert. Several studies indicated that S from Ginoux et al.(2001) over the Gobi Desert  
362 has been significantly underestimated and needs to be improved (Su and Fung, 2015; Zeng et al., 2020). Wu and Lin (2014)  
363 have demonstrated that the potential source regions in the southeast of Mongolia and the middle-east of Inner Mongolia  
364 are not well characterized by the S from GOCART scheme, which results in the underestimation of dust concentration in  
365 this area and its downwind regions. In addition, the source function may not provide precise enough information about the  
366 recent expansion of dust source areas over northern China, with the desertification and deforestation (Ku and Park, 2013).  
367 Studies have demonstrated that implementing a physically based parameterization instead of an empirical dust source  
368 function which is usually time-invariant and lacks physical treatment (Kok et al., 2014a, 2014b), or adopting the dynamic  
369 dust source function (Xi et al., 2015), could improve the representation of dust emission. Therefore, the dust source function  
370 should be precisely established with new updates and higher resolution using various measurements.

371 In terms of sandblasting efficiency  $\alpha$ , many modeling studies as well as observational analysis have investigated its  
372 magnitude and expression, but the results may vary greatly (Kang et al., 2011; Ma et al., 2019). The formulation for  $\alpha$  used

373 in our improved scheme is based on LS99, which establishes the relationship between  $\alpha$  and  $u_*$ , along with other soil-  
374 related parameters dependent on soil textures. In this study, we derived  $\alpha$  for different soil types based on the reported  
375 values, but uncertainties still remain due to limited available measurements. In addition to the expression from MB95 and  
376 LS99, there are other  $\alpha$  formulations proposed by Shao et al. (1996) (Shao96) and Shao04. Different from the empirical  
377 function, expressions of Shao96 and Shao04 are more sophisticated, which is the function of  $u_{*t}$  and  $u_*$  respectively,  
378 along with some size information of soil particles. Comparisons of different formulations of  $\alpha$  for different soil types (Kang  
379 et al., 2011; Ma et al., 2019) have shown that the variation in  $\alpha$  can reach up to several orders of magnitude, and few  
380 equations could reproduce the measured positive correlation between  $\alpha$  and  $u_*$ , suggesting that  $\alpha$  for different soil texture  
381 should be further investigated and observed to improve the model accuracy.

382 In this study, surface conditions including erodibility factor, soil texture, clay content and surface roughness length  
383 play a significant role in improving the model performance of  $u_*$ ,  $u_{*t}$  and  $F$ . We conclude that substituting globally fixed  
384 values of these properties with more realistic and physical-based ones could reduce the model uncertainty and improve the  
385 understanding of dust emission mechanism. In physically-based scheme, the importance of accurate input surface  
386 properties, including soil particle size distribution (Darmenova et al., 2009; Kok, 2011a, 2011b), soil texture (Shao et al.,  
387 2011; Foroutan et al., 2017), surface roughness length (Darmenova et al., 2009; Kontos et al., 2018) and soil plastic pressure  
388 (Lu and Shao, 1999; Kang et al., 2011), have also been highlighted by many studies. Therefore, accurate and abundant  
389 observation data of soil-related properties are urgently needed, particularly over dust source region. Moreover, various and  
390 comprehensive observation methods (e.g., experimental data, field and satellite observations) are recommended in order  
391 to correct and update the input data.

#### 392 **4 Summary and Conclusion**

393 In this study, we revised the treatments of dust emission processes by considering the effect of soil moisture, surface  
394 roughness, soil texture, as well as Owen effect and more physically-based formulation of sandblasting efficiency in GEOS-  
395 Chem version 12.6.0, in order to improve dust simulation over China. Several sensitivity simulations were conducted  
396 during a severe dust storm between March 27, 2015 to April 2, 2015 over northern China to analyze the effects of these  
397 modifications on  $u_*$ ,  $u_{*t}$  and emission flux.

398 In the improved scheme, we substituted global constant value of  $Z_0$ , assumed  $M_{\text{clay}}$  in the original version with  
399 geographical variation map obtained from the measurement provided by Prigent et al. (2005) and Shangguan et al. (2014)  
400 respectively.  $Z_{0s}$  and sandblasting efficiency were calculated with formulations based on soil texture data from FAO dataset,  
401 which is more physically-based than the original version. In addition, Owen effect and drag partition correction factor were  
402 considered in the improved version.

403 Sensitivity result showed that the modified  $f_d$  and  $f_w$  by inclusion of the updated  $Z_0$ ,  $Z_{0s}$  and  $M_{\text{clay}}$  resulted in  
404 significant alteration in  $u_{*t}$  (ranging from -8%~72%) over China.  $u_{*t}$  was increased when including the drag partition  
405 effect, particularly with the updated  $Z_0$  and  $Z_{0s}$  field (increased by 10%~60%), which induced the modeled  $u_{*t}$  much  
406 closer to the measurements. Considering Owen effect increased modeled  $u_*$  by 0%~39%, especially over northwest China  
407 where surface wind is strong. In general, modeled  $u_*$  was increased by 5%~50% over most parts of China due to the  
408 inclusion of Owen effect and updated  $Z_0$ . In terms of sandblasting efficiency, it was decreased by 50% on average with  
409 the updated  $u_*$ -dependent-ratio following LS99, with the largest reduction occurring over regions with sand texture. Due  
410 to the combined effect of updated treatments, emission flux simulated by improved scheme was generally decreased over  
411 northern China, except in some regions of northwest China, where Owen effect played a dominant role. Better agreement  
412 between the improved model results and observational values was achieved in terms of the  $u_{*t}$  and surface  $\text{PM}_{10}$   
413 concentrations in selected typical sites over northern China.

414 Compared with both surface  $\text{PM}_{10}$  observations and MODIS AOD, the revised dust emission scheme produced better  
415 performance in both temporal and spatial variation. Result showed that the dust concentrations were generally

416 underestimated at selected sites in the original scheme, particularly when dust concentrations were high. For the improved  
417 scheme, both the magnitude and the temporal evolution of PM<sub>10</sub> concentrations were well captured, with peak values much  
418 closer to the observations. According to the statistics, with the implementation of the updates, averaged PM<sub>10</sub> values at  
419 selected sites were more comparable to the observations, and the average MB and NMB values were reduced from -  
420 196.29 μg m<sup>-3</sup> and -52.79% in Control run to -47.72 μg m<sup>-3</sup> and -22.46% respectively. However, for some sites closer to  
421 Gobi desert, dust concentrations were still underestimated, which was likely attributed to the uncertainty in the erodibility  
422 factor over Gobi desert. Comparison of the model results and observed averaged PM<sub>10</sub> concentrations at ~1000 stations  
423 showed that the revised scheme improved the model performance, with R values increasing from 0.6 to 0.7, NMB values  
424 changing from -16% to -11%. Moreover, the improved scheme demonstrated better performance in reproducing the spatial  
425 distribution of AOD than the original scheme, particularly over the desert region of northwest China.

426 In summary, this study indicated that compared to the original scheme, the revised dust emission scheme had an  
427 overall better agreement with the measurements. However, more physically-based schemes and more detailed up-to-date  
428 input parameters should be further investigated and observed to improve the accuracy of model.

429 *Code and data availability:* Measurements used in this work have been listed in Sect. 2.4 and acknowledgements. For  
430 the model outputs and codes can be accessed by contacting Rong Tian (rongtian@nuist.edu.cn).

431 *Competing interests.* The authors declare that they have no conflict of interest.

432 *Author contributions.* RT designed and conducted the model experiments, analyzed the result and wrote the paper. XYM  
433 supervised the project, proposed scientific suggestions and revised the paper. JQZ processed the observation data.

434 *Acknowledgements.* This study is supported by the National Natural Science Foundation of China grants ([41675004](#)  
435 [41975002](#) & [4206113400941975002](#)), the National Key R&D Program of China grants (2019YFA0606802 &  
436 2016YFA0600404), [the Second Tibetan Plateau Scientific Expedition and Research \(STEP\) program \(2019QZKK0103\)](#),  
437 and the Postgraduate Research & Practice Innovation Program of Jiangsu Province (grant no. SJKY19\_0962). We are  
438 thankful to C. Prigent for kindly providing the input map of global surface aerodynamic roughness length Z<sub>0</sub>; to Shangguan  
439 W. for providing the soil clay content data, which is available from the website of Land-Atmospheric Interaction Research  
440 Group at Beijing Normal University (<http://globalchange.bnu.edu.cn/research/soilw#download>); to Sujan Koirala for  
441 providing global soil texture map which can be downloaded at the website ([http://hydro.iis.u-](http://hydro.iis.u-tokyo.ac.jp/~sujan/research/gswp3/soil-texture-map.html)  
442 [tokyo.ac.jp/~sujan/research/gswp3/soil-texture-map.html](http://hydro.iis.u-tokyo.ac.jp/~sujan/research/gswp3/soil-texture-map.html)). We are also grateful to GEOS-Chem Support Team for their  
443 management and maintenance of GEOS-Chem model. We acknowledge to NASA, Chinese Ministry of Environmental  
444 Protection and Chinese National Meteorological Center for providing the MODIS datasets, surface PM<sub>10</sub> observations and  
445 meteorological measurements respectively.

#### 446 **Reference:**

447 Alfaro, S. C. and Gomes, L.: Modelling mineral aerosol production by wind erosion: Emission intensities and aerosol size distributions  
448 in source areas, J. Geophys. Res., 106, 18075–18084, 2001.

449 Astitha, M., Lelieveld, J., Abdel Kader, M., Pozzer, A. and de Meij, A.: Parameterization of dust emissions in the global atmospheric  
450 chemistry-climate model EMAC: impact of nudging and soil properties, *Atmos. Chem. Phys.*, 12(22), 11057–11083,  
451 doi:10.5194/acp-12-11057-2012, 2012.

452 Bonan, G. B., A land surface model (LSM version 1.0) for ecological, hydrological, and atmospheric studies: Technical description and  
453 user's guide, Tech. Rep. NCAR TN – 417+STR, Natl. Cent. for Atmos. Res., Boulder, Colo., 1996.

454 Chen, D., Wang, Y., McElroy, M. B., He, K., Yantosca, R. M., and Le Sager, P.: Regional CO pollution and export in China simulated  
455 by the high-resolution nested-grid GEOS-Chem model, *Atmos. Chem. Phys.*, 9, 3825-3839, 10.5194/acp-9-3825-2009, 2009.

456 Chen, L., Gao, Y., Zhang, M., Fu, J. S., Zhu, J., Liao, H., Li, J., Huang, K., Ge, B., Wang, X., Lam, Y. F., Lin, C.-Y., Itahashi, S.,  
457 Nagashima, T., Kajino, M., Yamaji, K., Wang, Z. and Kurokawa, J.: MICS-Asia III: multi-model comparison and evaluation of  
458 aerosol over East Asia, *Atmos. Chem. Phys.*, 19(18), 11911–11937, doi:10.5194/acp-19-11911-2019, 2019.

459 Chen, S., Huang, J., Qian, Y., Zhao, C., Kang, L., Yang, B., Wang, Y., Liu, Y., Yuan, T., Wang, T., Ma, X. and Zhang, G.: An overview  
460 of mineral dust modeling over East Asia, *J Meteorol Res*, 31(4), 633–653, doi:10.1007/s13351-017-6142-2, 2017.

461 Chen, S., Zhao, C., Qian, Y., Leung, L. R., Huang, J., Huang, Z., Bi, J., Zhang, W., Shi, J., Yang, L., Li, D. and Li, J.: Regional modeling  
462 of dust mass balance and radiative forcing over East Asia using WRF-Chem, *Aeolian Research*, 15, 15–30,  
463 doi:10.1016/j.aeolia.2014.02.001, 2014.

464 Cheng, T., Peng, Y., Feichter, J. and Tegen, I.: An improvement on the dust emission scheme in the global aerosol-climate model  
465 ECHAM5-HAM, *Atmos. Chem. Phys.*, 13, 2008.

466 Cheng, Y., Zheng, G., Wei, C., Mu, Q., Zheng, B., Wang, Z., Gao, M., Zhang, Q., He, K., and Carmichael, G.: Reactive nitrogen  
467 chemistry in aerosol water as a source of sulfate during haze events in China, *Science Advances*, 2, e1601530,  
468 https://doi.org/10.1126/sciadv.1601530, 2016.

469 Chin, M., Diehl, T., Tan, Q., Prospero, J. M., Kahn, R. A., Remer, L. A., Yu, H., Sayer, A. M., Bian, H., Geogdzhayev, I. V., Holben,  
470 B. N., Howell, S. G., Huebert, B. J., Hsu, N. C., Kim, D., Kucsera, T. L., Levy, R. C., Mishchenko, M. I., Pan, X., Quinn, P. K.,  
471 Schuster, G. L., Streets, D. G., Strode, S. A., Torres, O., and Zhao, X.-P.: Multi-decadal aerosol variations from 1980 to 2009: a  
472 perspective from observations and a global model, *Atmos. Chem. Phys.*, 14, 3657–3690, https://doi.org/10.5194/acp-14-3657-2014,  
473 2014.

474 Darnenova, K., Sokolik, I. N., Shao, Y., Marticorena, B., and Bergametti, G.: Development of a physically based dust emission module  
475 within the Weather Research and Forecasting (WRF) model: Assessment of dust emission parameterizations and input parameters  
476 for source regions in Central and East Asia, *J. Geophys. Res.*, 114, D14201, doi:10.1029/2008JD011236, 2009.

477 DeMott, P. J., Sassen, K., Poellot, M. R., Baumgardner, D., Rogers, D. C., Brooks, S. D., Prenni, A. J., and Kreidenweis, S. M. African  
478 dust aerosols as atmospheric ice nuclei, *Geophys. Res. Lett.*, 30, 1732, doi:10.1029/2003gl017410, 2003.

479 DeMott, P. J., Prenni, A. J., Liu, X., Kreidenweis, S. M., Petters, M. D., Twohy, C. H., Richardson, M. S., Eidhammer, T., and  
480 Rodgers, D. C.: Predicting global atmospheric ice nuclei distributions and their impacts on climate, *P. Natl. Acad. Sci. USA*, 107,  
481 11217–11222, 2010.

482 Fairlie, T. D., Jacob, D. J., and Park, R. J.: The impact of transpacific transport of mineral dust in the United States, *Atmos. Environ.*,  
483 41, 1251–1266, 2007.

484 Fecan, F., Marticorena, B., and Bergametti, G.: Parametrization of the increase of the aeolian erosion threshold wind friction velocity  
485 due to soil moisture for arid and semi-arid areas, *Ann. Geophys.*, 17, 149–157, doi:10.1007/s00585-999-0149-7, 1999.

486 Foroutan, H., Young, J., Napelenok, S., Ran, L., Appel, K. W., Gilliam, R. C. and Pleim, J. E.: Development and evaluation of a physics-  
487 based windblown dust emission scheme implemented in the CMAQ modeling system: WINDBLOWN DUST IN CMAQ, *J. Adv.*  
488 *Model. Earth Syst.*, 9(1), 585–608, doi:10.1002/2016MS000823, 2017.

489 Gherboudj, I., Beegum, S. N., Marticorena, B. and Ghedira, H.: Dust emission parameterization scheme over the MENA region:  
490 Sensitivity analysis to soil moisture and soil texture: DUST EMISSION OVER MENA REGION, *J. Geophys. Res. Atmos.*, 120(20),  
491 10,915-10,938, doi:10.1002/2015JD023338, 2015.

492 Giannadaki, D., Pozzer, A., and Lelieveld, J.: Modeled global effects of airborne desert dust on air quality and premature mortality,

493 Atmos. Chem. Phys., 14, 957–968, <https://doi.org/10.5194/acp-14-957-2014>, 2014.

494 Gillette, D. A., Fryrear, D. W., Gill, T. E., Ley, T., Cahill, T. A., and Gearhart, E. A.: Relation of vertical flux of particles smaller than  
495 10  $\mu\text{m}$  to total aeolian horizontal mass flux at Owens Lake, *J. Geophys. Res.-Atmos.*, 102, 26009–26015,  
496 <https://doi.org/10.1029/97JD02252>, 1997.

497 Ginoux, P., Chin, M., Tegen, I., Prospero, J. M., Holben, B., Dubovik, O. and Lin, S.-J.: Sources and distributions of dust aerosols  
498 simulated with the GOCART model, *J. Geophys. Res.*, 106(D17), 20255–20273, doi:10.1029/2000JD000053, 2001.

499 Ginoux, P., Prospero, J. M., Torres, O., and Chin, M.: Long-term simulation of global dust distribution with the GOCART model:  
500 correlation with North Atlantic Oscillation, *Environmental Model. Soft.*, 19, 113–128, 2004.

501 Gomes, L., Arrúe, J. L., López, M. V., Sterk, G., Richard, D., Gracia, R., Sabre, M., Gaudichet, A. and Frangi, J. P.: Wind erosion in a  
502 semiarid agricultural area of Spain: the WELSONS project, *CATENA*, 52(3–4), 235–256, doi:10.1016/S0341-8162(03)00016-X,  
503 2003.

504 Goudie, A. S.: Desert dust and human health disorders, *Environ. Int.*, 63, 101–113, <https://doi.org/10.1016/j.envint.2013.10.011>, 2014.

505 Huneus, N., Schulz, M., Balkanski, Y., Griesfeller, J., Prospero, J., Kinne, S., Bauer, S., Boucher, O., Chin, M., Dentener, F., Diehl, T.,  
506 Easter, R., Fillmore, D., Ghan, S., Ginoux, P., Grini, A., Horowitz, L., Koch, D., Krol, M. C., Landing, W., Liu, X., Mahowald, N.,  
507 Miller, R., Morcrette, J.-J., Myhre, G., Penner, J., Perlwitz, J., Stier, P., Takemura, T., and Zender, C. S.: Global dust model  
508 intercomparison in AeroCom phase I, *Atmos. Chem. Phys.*, 11, 7781–7816, doi:10.5194/acp-11-7781-2011, 2011.

509 Iversen, J. D. and White, B. R.: Saltation threshold on Earth, Mars and Venus, *Sedimentology*, 29(1), 111–119, doi:10.1111/j.1365-  
510 3091.1982.tb01713.x, 1982.

511 Ju, T., Li, X., Zhang, H., Cai, X., and Song, Y.: Comparison of two different dust emission mechanisms over the Horqin Sandy Land  
512 area: Aerosols contribution and size distributions, *Atmos. Environ.*, 176, 82–90, <https://doi.org/10.1016/j.atmosenv.2017.12.017>,  
513 2018.

514 Kang, J.-Y., Yoon, S.-C., Shao, Y. and Kim, S.-W.: Comparison of vertical dust flux by implementing three dust emission schemes in  
515 WRF/Chem, *J. Geophys. Res.*, 116(D9), D09202, doi:10.1029/2010JD014649, 2011.

516 Klingmüller, K., Metzger, S., Abdelkader, M., Karydis, V. A., Stenchikov, G. L., Pozzer, A. and Lelieveld, J.: Revised mineral dust  
517 emissions in the atmospheric chemistry–climate model EMAC (MESSy 2.52 DU\_Astithal KKDU2017 patch), *Geosci. Model Dev.*,  
518 11(3), 989–1008, doi:10.5194/gmd-11-989-2018, 2018.

519 Kok, J. F.: Does the size distribution of mineral dust aerosols depend on the wind speed at emission?, *Atmos. Chem. Phys.*, 11, 10149–  
520 10156, doi:10.5194/acp-11-10149-2011, 2011a.

521 Kok, J. F.: A scaling theory for the size distribution of emitted dust aerosols suggests climate models underestimate the size of the global  
522 dust cycle, *Proc. Natl. Acad. Sci. USA*, 108, 1016–1021, 2011b.

523 Kok, J. F., Mahowald, N. M., Fratini, G., Gillies, J. A., Ishizuka, M., Leys, J. F., Mikami, M., Park, M.-S., Park, S.-U., Van Pelt, R. S.  
524 and Zobeck, T. M.: An improved dust emission model – Part 1: Model description and comparison against measurements, *Atmos.*  
525 *Chem. Phys.*, 14(23), 13023–13041, doi:10.5194/acp-14-13023-2014, 2014a.

526 Kok, J. F., Albani, S., Mahowald, N. M. and Ward, D. S.: An improved dust emission model – Part 2: Evaluation in the Community  
527 Earth System Model, with implications for the use of dust source functions, *Atmos. Chem. Phys.*, 14(23), 13043–13061,  
528 doi:10.5194/acp-14-13043-2014, 2014b.

529 Kontos, S., Liora, N., Giannaros, C., Kakosimos, K., Poupkou, A. and Melas, D.: Modeling natural dust emissions in the central Middle  
530 East: Parameterizations and sensitivity, *Atmospheric Environment*, 190, 294–307, doi:10.1016/j.atmosenv.2018.07.033, 2018.

531 Ku, B. and Park, R. J.: Comparative inverse analysis of satellite (MODIS) and ground (PM10) observations to estimate dust emissions  
532 in East Asia, *Asia-Pacific J Atmos Sci*, 49(1), 3–17, doi:10.1007/s13143-013-0002-5, 2013.

533 Kumar, R., Barth, M. C., Pfister, G. G., Naja, M., and Brasseur, G. P.: WRF-Chem simulations of a typical premonsoon dust storm in  
534 northern India: influences on aerosol optical properties and radiation budget, *Atmos. Chem. Phys.*, 14, 2431–2446,  
535 <https://doi.org/10.5194/acp-14-2431-2014>, 2014.

536 Latimer, R.N.C., and R.V. Martin, Interpretation of measured aerosol mass scattering efficiency over North America using a chemical

537 transport model, *Atmos. Chem. Phys.*, 19, 2635–2653, 2019.

538 Laurent, B., Marticorena, B., Bergametti, G., Chazette, P., Maignan, F., and Schmechtig, C.: Simulation of the mineral dust emission  
539 frequencies from desert areas of China and Mongolia using an aerodynamic roughness length map derived from the  
540 POLDER/ADEOS-1 surface products, *J. Geophys. Res.*, 110, D18S04, doi:10.1029/2004JD005013, 2005.

541 Laurent, B., Marticorena, B., Bergametti, G., and Mei, F.: Modeling mineral dust emissions from Chinese and Mongolian deserts, *Global  
542 Planet. Changes*, 52, 121–141, 2006.

543 Laurent, B., Marticorena, B., Bergametti, G., Leon, J.-F., and Mahowald, N.: Modeling mineral dust emissions from the Sahara desert  
544 using new surface properties and soil database, *J. Geophys. Res.*, VOL. 113, D14218, doi:10.1029/2007JD009484, 2008.

545 [Li, K., Jacob, D. J., Liao, H., Zhu, J., Shah, V., Shen, L., Bates, K. H., Zhang, Q. and Zhai, S.: A two-pollutant strategy for improving  
546 ozone and particulate air quality in China, \*Nat. Geosci.\*, 12\(11\), 906–910, <https://doi.org/10.1038/s41561-019-0464-x>, 2019.](#)

547 [Lin, J., Xin, J., Che, H., Wang, Y., and Donkelaar, A. V.: Clear-sky aerosol optical depth over East China estimated from visibility  
548 measurements and chemical transport modeling, \*Atmos. Environ.\*, 95, 258–267, 2014.](#)

549 Liu, D., Ishizuka, M., Mikami, M., and Shao, Y.: Turbulent characteristics of saltation and uncertainty of saltation model parameters,  
550 *Atmos. Chem. Phys.*, 18, 7595–7606, <https://doi.org/10.5194/acp-18-7595-2018>, 2018.

551 Liu, H., Jacob, D. J., Bey, I., and Yantosca, R. M.: Constraints from <sup>210</sup>Pb and <sup>7</sup>Be on wet deposition and transport in a global three-  
552 dimensional chemical tracer model driven by assimilated meteorological fields, *J. Geophys. Res.*, 106, 12109–12128,  
553 doi:10.1029/2000JD900839, 2001.

554 Lu, H. and Shao, Y.: A new model for dust emission by saltation bombardment, *J. Geophys. Res.*, 104(D14), 16827–16842,  
555 doi:10.1029/1999JD900169, 1999.

556 Ma, S., Zhang, X., Gao, C., Tong, D. Q., Xiu, A., Wu, G., Cao, X., Huang, L., Zhao, H., Zhang, S., Ibarra-Espinosa, S., Wang, X., Li,  
557 X. and Dan, M.: Multimodel simulations of a springtime dust storm over northeastern China: implications of an evaluation of four  
558 commonly used air quality models (CMAQ v5.2.1, CAMx v6.5.0, CHIMERE v2017r4, and WRF-Chem v3.9.1), *Geosci. Model  
559 Dev.*, 12(11), 4603–4625, doi:10.5194/gmd-12-4603-2019, 2019.

560 Macpherson, T., Nickling, W. G., Gillies, J. A. and Etyemezian, V.: Dust emissions from undisturbed and disturbed supply-limited desert  
561 surfaces, *J. Geophys. Res.*, 113(F2), F02S04, doi:10.1029/2007JF000800, 2008.

562 Mahowald, N. and Kiehl, L.: Mineral aerosol and cloud interactions, *Geophys. Res. Lett.*, 30, 1475, doi:10.1029/2002GL016762, 2003.

563 Marticorena, B. and Bergametti, G.: Modeling the atmospheric dust cycle: 1. Design of a soil-derived dust emission scheme, *J. Geophys.  
564 Res.*, 100(D8), 16415, doi:10.1029/95JD00690, 1995.

565 Menut, L., Pérez, C., Haustein, K., Bessagnet, B., Prigent, C. and Alfaro, S.: Impact of surface roughness and soil texture on mineral  
566 dust emission fluxes modeling: IMPACT OF ROUGHNESS AND SOIL TEXTURE ON MINERAL DUST, *J. Geophys. Res.*  
567 *Atmos.*, 118(12), 6505–6520, doi:10.1002/jgrd.50313, 2013.

568 Mokhtari, M., Gomes, L., Tulet, P. and Rezoug, T.: Importance of the surface size distribution of erodible material: an improvement on  
569 the Dust Entrainment And Deposition (DEAD) Model, *Geosci. Model Dev.*, 5(3), 581–598, doi:10.5194/gmd-5-581-2012, 2012.

570 Nagashima, K., Suzuki, Y., Irino, T., Nakagawa, T., Tada, R., Hara, Y., Yamada, K. and Kurosaki, Y.: Asian dust transport during the  
571 last century recorded in Lake Suigetsu sediments, *Geophys. Res. Lett.*, 43(6), 2835–2842, doi:10.1002/2015GL067589, 2016.

572 Owen, P. R., Saltation of uniform grains in air, *J. Fluid Mech.*, 20, 225–242, 1964.

573 Panebianco, J. E., Mendez, M. J. and Buschiazzo, D. E.: PM10 Emission, Sandblasting Efficiency and Vertical Entrainment During  
574 Successive Wind-Erosion Events: A Wind-Tunnel Approach, *Boundary-Layer Meteorol.*, 161(2), 335–353, doi:10.1007/s10546-  
575 016-0172-7, 2016.

576 Perlwitz, J. P., Pérez García-Pando, C., and Miller, R. L.: Predicting the mineral composition of dust aerosols – Part 1: Representing key  
577 processes, *Atmos. Chem. Phys.*, 15, 11593–11627, <https://doi.org/10.5194/acp-15-11593-2015>, 2015a.

578 Perlwitz, J. P., Pérez García-Pando, C., and Miller, R. L.: Predicting the mineral composition of dust aerosols – Part 2: Model evaluation  
579 and identification of key processes with observations, *Atmos. Chem. Phys.*, 15, 11629–11652, [https://doi.org/10.5194/acp-15-  
580 11629-2015](https://doi.org/10.5194/acp-15-11629-2015), 2015b.

581 Prigent, C., Tegen, I., Aires, F., Marticorena, B., and Zribi M.: Estimation of the aerodynamic roughness length in arid and semiarid  
582 regions over the globe with the ERS scatterometer, *J. Geophys. Res.*, 110, D09205, doi:10.1029/2004JD005370, 2005.

583 Prigent, C., Jiménez, C. and Catherinot, J.: Comparison of satellite microwave backscattering (ASCAT) and visible/near-infrared  
584 reflectances (PARASOL) for the estimation of aeolian aerodynamic roughness length in arid and semi-arid regions, *Atmos. Meas.*  
585 *Tech.*, 5(11), 2703–2712, doi:10.5194/amt-5-2703-2012, 2012.

586 Rajot, J. L., Alfaro, S. C., Gomes, L. and Gaudichet, A.: Soil crusting on sandy soils and its influence on wind erosion, *CATENA*, 53(1),  
587 1–16, doi:10.1016/S0341-8162(02)00201-1, 2003.

588 Ridley, D. A., Heald, C. L., and Ford, B.: North African dust transport and deposition: a satellite and model perspective, *J. Geophys.*  
589 *Res.*, 117, D02202, doi:10.1029/2011JD016794, 2012.

590 Ridley, D. A., Heald, C. L., Kok, J. F. and Zhao, C.: An observationally constrained estimate of global dust aerosol optical depth, *Atmos.*  
591 *Chem. Phys.*, 16(23), 15097–15117, doi:10.5194/acp-16-15097-2016, 2016.

592 Roney, J. A. and White, B. R.: Estimating fugitive dust emission rates using an environmental boundary layer wind tunnel, *Atmospheric*  
593 *Environment*, 40(40), 7668–7685, doi:10.1016/j.atmosenv.2006.08.015, 2006.

594 Saidou Chaibou, A. A., Ma, X. and Sha, T.: Dust radiative forcing and its impact on surface energy budget over West Africa, *Sci Rep*,  
595 10(1), 12236, doi:10.1038/s41598-020-69223-4, 2020a.

596 Saidou Chaibou, A. A., Ma, X., Kumar, K. R., Jia, H., Tang, Y. and Sha, T.: Evaluation of dust extinction and vertical profiles simulated  
597 by WRF-Chem with CALIPSO and AERONET over North Africa, *Journal of Atmospheric and Solar-Terrestrial Physics*, 199,  
598 105213, doi:10.1016/j.jastp.2020.105213, 2020b.

599 Shangguan, W., Dai, Y., Duan, Q., Liu, B. and Yuan, H.: A global soil data set for earth system modeling, *J. Adv. Model. Earth Syst.*,  
600 6(1), 249–263, doi:10.1002/2013MS000293, 2014.

601 Shao, Y.: A model for mineral dust emission, *J. Geophys. Res.*, 106, 20239–20254, <https://doi.org/10.1029/2001JD900171>, 2001.

602 Shao, Y.: Simplification of a dust emission scheme and comparison with data, *J. Geophys. Res.*, 109, D10202,  
603 <https://doi.org/10.1029/2003JD004372>, 2004.

604 Shao, Y., Ishizuka, M., Mikami, M., and Leys, J. F.: Parameterization of size-resolved dust emission and validation with measurements,  
605 *J. Geophys. Res.*, 116, D08203, doi:10.1029/2010JD014527, 2011.

606 Shao, Y. P., Raupach, M. R., and Leys, J. F.: A model for predicting aeolian sand drift and dust entrainment on scales from paddock to  
607 region, *Austr. J. Soil Res.*, 34, 309–342, 1996.

608 Su, L. and Fung, J. C. H.: Sensitivities of WRF-Chem to dust emission schemes and land surface properties in simulating dust cycles  
609 during springtime over East Asia: Simulated Dust Cycles Over East Asia, *J. Geophys. Res. Atmos.*, 120(21), 11,215-11,230,  
610 doi:10.1002/2015JD023446, 2015.

611 Tegen, I., A. L. Andrew, and I. Fung, The influence on climate forcing of mineral aerosols from disturbed soils, *Nature*, 380, 419–422,  
612 1996.

613 Tegen, I., Harrison, S. P., Kohfeld, K., Prentice, I. C., Coe, M., and Heimann, M.: Impact of vegetation and preferential source areas on  
614 global dust aerosol: Results from a model study, *J. Geophys. Res.-Atmos.*, 107, 4576, doi:10.1029/2001JD000963, 2002.

615 Tegen, I.: Modeling the mineral dust aerosol cycle in the climate system, *Quaternary Sci. Rev.*, 22, 1821–1834, 2003.

616 Tian, R., Ma, X., Jia, H., Yu, F., Sha, T. and Zan, Y.: Aerosol radiative effects on tropospheric photochemistry with GEOS-Chem  
617 simulations, *Atmospheric Environment*, 208, 82–94, doi:10.1016/j.atmosenv.2019.03.032, 2019.

618 Todd, M. C., Bou Karam, D., Cavazos, C., Bouet, C., Heinold, B., Baldasano, J. M., Cautenet, G., Koren, I., Perez, C., Solmon, F.,  
619 Tegen, I., Tulet, P., Washington, R., and Zakey, A.: Quantifying uncertainty in estimates of mineral dust flux: an intercomparison  
620 of model performance over the Bodele Depression, Northern Chad, *J. Geophys. Res.*, 113, D24107, doi:10.1029/2008JD010476,  
621 2008.

622 Tong, D. Q., Wang, J. X. L., Gill, T. E., Lei, H., and Wang, B.: Intensified dust storm activity and Valley fever infection in the  
623 southwestern United States, *Geophys. Res. Lett.*, 44, 4304–4312, <https://doi.org/10.1002/2017GL073524>, 2017.

624 Uno, I., Wang, Z., Chiba, M., Chun, Y. S., Gong, S. L., Hara, Y., Jung, E., Lee, S.-S., Liu, M., Mikami, M., Music, S., Nickovic, S.,

625 Satake, S., Shao, Y., Song, Z., Sugimoto, N., Tanaka, T. and Westphal, D. L.: Dust model intercomparison (DMIP) study over Asia:  
626 Overview, *J. Geophys. Res.*, 111(D12), D12213, doi:10.1029/2005JD006575, 2006.

627 Wang, C. Z., Niu, S. J., and Zhou, Y.: Recent progress on the observation study of wind erosion in China, *Meteorological Monthly*,  
628 11,107-116, 2009. (in Chinese)

629 [Wang, Y. X., Mcelroy, M. B., Jacob, D. J., and Yantosca, R. M.: A nested grid formulation for chemical transport over Asia: Applications  
630 to CO, \*J. Geophys. Res. Atmos.\*, 109, D22307, 10.1029/2004JD005237, 2004.](#)

631 [Wang, Y., Zhang, Q. Q., He, K., Zhang, Q., and Chai, L.: Sulfate-nitrate-ammonium aerosols over China: response to 2000–2015  
632 emission changes of sulfur dioxide, nitrogen oxides, and ammonia, \*Atmos. Chem. Phys.\*, 13, 2635-2652, 10.5194/acp-13-2635-  
633 2013, 2013.](#)

634 [Wang, Y., Zhang, Q., Jiang, J., Zhou, W., Wang, B., He, K., Duan, F., Zhang, Q., Philip, S. and Xie, Y.: Enhanced sulfate formation  
635 during China's severe winter haze episode in January 2013 missing from current models: MODELING WINTER HAZE  
636 FORMATION IN CHINA, \*J. Geophys. Res. Atmos.\*, 119\(17\), 10,425-10,440, <https://doi.org/10.1002/2013JD021426>, 2014.](#)

637 Wang, Z., Pan, X., Uno, I., Li, J., Wang, Z., Chen, X., Fu, P., Yang, T., Kobayashi, H., Shimizu, A., Sugimoto, N. and Yamamoto, S.:  
638 Significant impacts of heterogeneous reactions on the chemical composition and mixing state of dust particles: A case study during  
639 dust events over northern China, *Atmospheric Environment*, 159, 83–91, doi:10.1016/j.atmosenv.2017.03.044, 2017.

640 Wu, C.-L.: Improvements of Dust Emission Processes in CESM Model and Its Application, doctoral dissertation. University of Chinese  
641 Academy of Sciences, 2013. (in Chinese)

642 Wu, C. L. and Lin Z. H.: Impact of two different dust emission schemes on the simulation of a severe dust storm in East Asia using the  
643 WRF/Chem model, *Climatic and Environmental Research*, 19 (4): 419-436, 2014. (in Chinese)

644 Wu, M., Liu, X., Yang, K., Luo, T., Wang, Z., Wu, C., Zhang, K., Yu, H. and Darnenov, A.: Modeling Dust in East Asia by CESM and  
645 Sources of Biases, *J. Geophys. Res. Atmos.*, 124(14), 8043–8064, doi: 10.1029/2019JD030799, 2019.

646 Xi, X. and Sokolik, I. N.: Seasonal dynamics of threshold friction velocity and dust emission in Central Asia, *J. Geophys. Res. Atmos.*,  
647 120(4), 1536–1564, doi:10.1002/2014JD022471, 2015.

648 Zender, C. S., Bian, H., and Newman, D.: Mineral Dust Entrainment and Deposition (DEAD) model: Description and 1990s dust  
649 climatology, *J. Geophys. Res.*, 108, 4416, doi:10.1029/2002JD002775, 2003.

650 Zeng, Y., Wang, M., Zhao, C., Chen, S., Liu, Z., Huang, X. and Gao, Y.: WRF-Chem v3.9 simulations of the East Asian dust storm in  
651 May 2017: modeling sensitivities to dust emission and dry deposition schemes, *Geosci. Model Dev.*, 13(4), 2125–2147,  
652 doi:10.5194/gmd-13-2125-2020, 2020.

653 Zhang, L., Gong, S., Padro, J., and Barrie, L.: A size-segregated particle dry deposition scheme for an atmospheric aerosol module,  
654 *Atmos. Environ.*, 35, 549–560, 2001.

655 [Zhang, L., Kok, J. F., Henze, D. K., Li, Q. and Zhao, C.: Improving simulations of fine dust surface concentrations over the western  
656 United States by optimizing the particle size distribution: IMPROVING SIMULATED DUST OVER WESTERN US, \*Geophys.  
657 Res. Lett.\*, 40\(12\), 3270–3275, <https://doi.org/10.1002/grl.50591>, 2013.](#)

658 [Zhang, L., Liu, L., Zhao, Y., Gong, S., Zhang, X., Henze, D. K., Capps, S. L., Fu, T.-M., Zhang, Q., and Wang, Y.: Source attribution  
659 of particulate matter pollution over North China with the adjoint method, \*Environmental Research Letters\*, 10, 084011,  
660 \[10.1088/1748-9326/10/8/084011\]\(https://doi.org/10.1088/1748-9326/10/8/084011\), 2015.](#)

661 Zhang, J., Teng, Z., Huang, N., Guo, L. and Shao, Y.: Surface renewal as a significant mechanism for dust emission, *Atmos. Chem.  
662 Phys.*, 16(24), 15517–15528, doi:10.5194/acp-16-15517-2016, 2016.

663 Zhao, C., Chen, S., Leung, L. R., Qian, Y., Kok, J. F., Zaveri, R. A., and Huang, J.: Uncertainty in modeling dust mass balance and  
664 radiative forcing from size parameterization, *Atmos. Chem. Phys.*, 13, 10733–10753, <https://doi.org/10.5194/acp-13-10733-2013>,  
665 2013.

666 Zhao, C., Liu, X., and Leung, L. R.: Impact of the Desert dust on the summer monsoon system over Southwestern North America, *Atmos.  
667 Chem. Phys.*, 12, 3717–3731, <https://doi.org/10.5194/acp-12-3717-2012>, 2012.

668 Zhao, J., Ma, X., Wu, S. and Sha, T.: Dust emission and transport in Northwest China: WRF-Chem simulation and comparisons with



669 multi-sensor observations, *Atmospheric Research*, 241, 104978, doi:10.1016/j.atmosres.2020.104978, 2020.  
670 Zheng, B., Zhang, Q., Zhang, Y., He, K. B., Wang, K., Zheng, G. J., Duan, F. K., Ma, Y. L., and Kimoto, T.: Heterogeneous chemistry:  
671 a mechanism missing in current models to explain secondary inorganic aerosol formation during the January 2013 haze episode in  
672 North China, *Atmos. Chem. Phys.*, 15, 2031–2049, <https://doi.org/10.5194/acp-15-2031-2015>, 2015.  
673

674 Table 1. Input soil aggregate size distribution parameters dependent on soil texture classification following USDA.

Soil Texture	Mode1			Mode2			Mode3			$Z_{0s}$
	n	MMD	$\sigma$	n	MMD	$\sigma$	n	MMD	$\sigma$	
Sand	0.9	1000	1.6	0.1	100	1.7	0	10	1.8	$33.3 \times 10^{-4}$
Loamy sand	0.6	690	1.6	0.3	100	1.7	0.1	10	1.8	$23 \times 10^{-4}$
Sandy loam	0.6	520	1.6	0.3	100	1.7	0.1	5	1.8	$17.3 \times 10^{-4}$
Silt loam	0.5	520	1.6	0.35	100	1.7	0.15	5	1.8	$17.3 \times 10^{-4}$
Loam	0.35	520	1.6	0.5	75	1.7	0.15	2.5	1.8	$17.3 \times 10^{-4}$
Sandy clay loam	0.3	210	1.7	0.5	75	1.7	0.2	2.5	1.8	$7 \times 10^{-4}$
Silt clay loam	0.3	210	1.7	0.5	50	1.7	0.2	2.5	1.8	$7 \times 10^{-4}$
Clay loam	0.2	125	1.7	0.5	50	1.7	0.3	1	1.8	$4.2 \times 10^{-4}$
Sandy clay	0.65	100	1.8	0	10	1.8	0.35	1	1.8	$3.3 \times 10^{-4}$
Silty clay	0.6	100	1.8	0	10	1.8	0.4	0.5	1.8	$3.3 \times 10^{-4}$
Clay	0.5	100	1.8	0	10	1.8	0.5	0.5	1.8	$3.3 \times 10^{-4}$
Silt	0.45	520	1.6	0.4	75	1.7	0.15	2.5	1.8	$17.3 \times 10^{-4}$

675 Including three-mode log-normal parameters (mass fraction n (%), mass median diameter MMD ( $\mu\text{m}$ ), and geometric standard deviation  
676  $\sigma$ ), and smooth aeolian roughness length  $z_{0s}$  ( $\mu\text{cm}$ ).

677 Table 2. Input soil-related parameters for different soil texture used in calculation of sandblasting efficiency  $\alpha$ .

Soil Texture	$p(N\text{ m}^{-2})$	$f(\%)$	$\rho_b(\text{kg m}^{-3})$	$C_\alpha$
Sand	5000	6.9	1000	0.01
Loamy sand	5000	18.5	1000	0.008
Sandy loam	10000	22.3	800	0.7
Silt loam	10000	22.3	800	0.7
Loam	10000	22.3	800	0.7
Sandy clay loam	10000	22.3	800	0.9
Silt clay loam	10000	22.3	800	0.7
Clay loam	10000	22.3	800	0.9
Sandy clay	30000	72	700	0.2
Silty clay	30000	72	700	0.2
Clay	30000	72	700	0.2
Silt	10000	22.3	800	0.9

678

679 Table 3. Sensitivity Experiments design and description.

Experiment name	Modifications					Description
	Updated $M_{\text{clay}}$	Owen effect	Updated $\alpha$	Drag partition correction (Default $Z_0$ , $Z_{0s}$ )	Updated $Z_0$ , $Z_{0s}$	
Control	N	N	N	N	N	Original scheme with default configurations. Serves as a control simulation.
Sen_mclay	Y	N	N	N	N	Adopting global $M_{\text{clay}}$ from Shangguan et al. (2014).
Sen_owen	N	Y	N	N	N	Considering Owen effect.
Sen_ratio	N	N	Y	N	N	Using updated $\alpha$ from Lu and Shao (1999).
Sen_drag	N	N	N	Y	N	Considering $f_d$ but with $Z_0=0.01$ cm, $Z_{0s}=0.0033$ cm
Sen_ $Z_0Z_{0s}$	N	N	N	N	Y	Using updated $Z_0$ from Prigent et al. (2005) and updated $Z_{0s}$ .
Sen_all	Y	Y	Y	Y	Y	Improved scheme including all the modifications described above.

680

681 Table 4. Statistics for observed and simulated (Control and Sen\_all) surface  $PM_{10}$  concentrations at selected sites.

Sites	Obs mean ( $\mu\text{g m}^{-3}$ )	Mod mean ( $\mu\text{g m}^{-3}$ )		R		MB ( $\mu\text{g m}^{-3}$ )		NMB (%)	
		Control	Sen_all	Control	Sen_all	Control	Sen_all	Control	Sen_all
Beijing	232.33	130.54	148.90	0.17	0.15	-87.40	-64.78	-37.62	-27.88
Tianjin	196.68	121.86	135.89	0.01	0.02	-72.87	-52.46	-37.05	-26.67
Huhehaote	148.35	108.76	119.88	0.67	0.66	-39.02	-27.49	-26.30	-18.53
Xilinguole	116.51	48.35	64.11	0.56	0.57	-72.47	-73.17	-62.20	-62.80
Kuele	487.96	163.88	559.67	0.57	0.55	-315.26	123.77	-64.61	25.37
Hami	238.74	146.58	453.88	0.64	0.81	-163.50	-50.57	-68.48	-21.18
Akesu	738.39	236.09	827.03	0.45	0.50	-503.61	79.95	-68.20	10.83
Jiuquan	653.77	320.55	464.01	0.19	0.34	-338.29	-227.17	-51.74	-34.75
Baiyin	295.84	120.45	155.93	0.46	0.69	-174.16	-137.55	-58.87	-46.50
Average	345.40	155.23	325.48	0.41	0.48	-196.29	-47.72	-52.79	-22.46

682

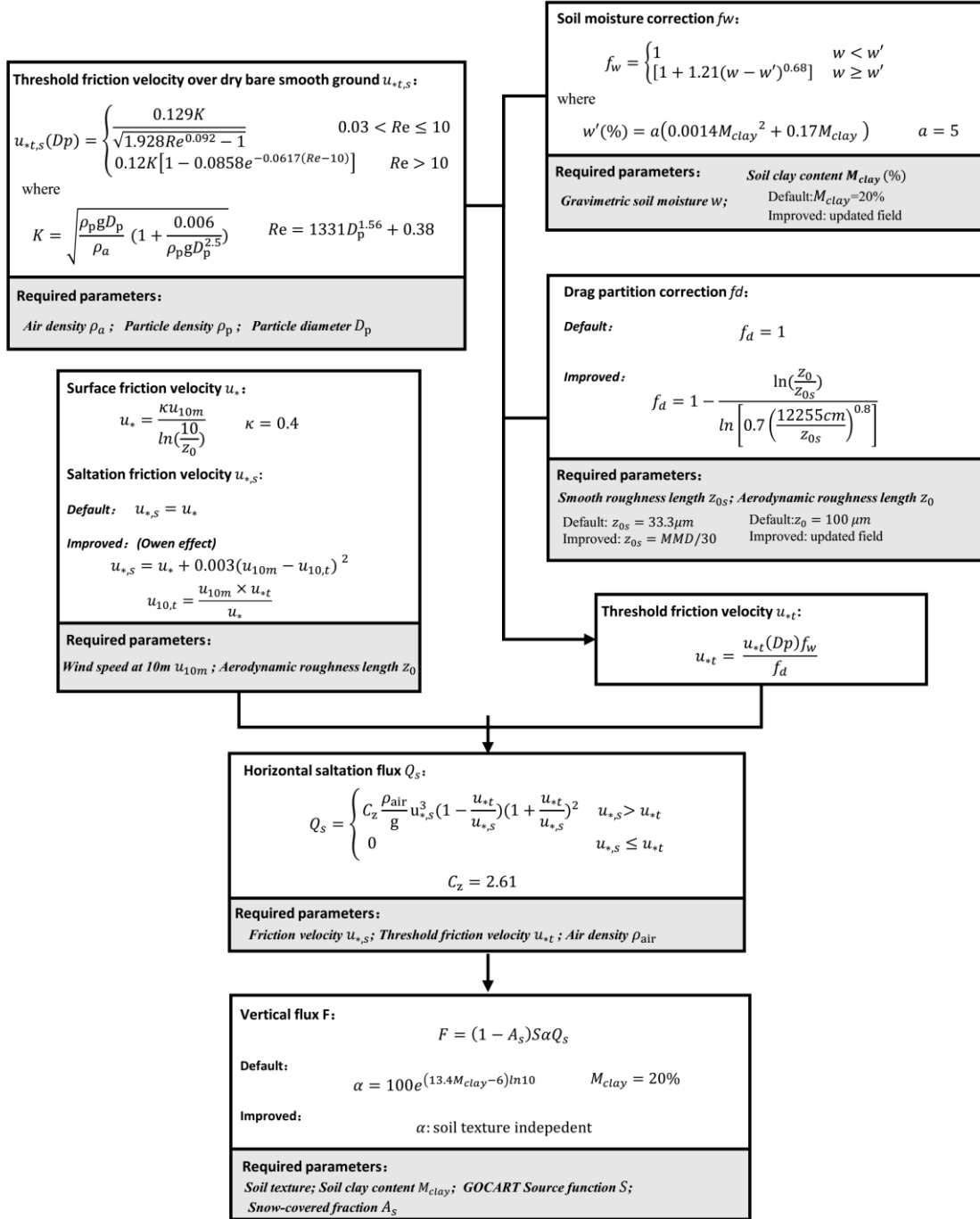
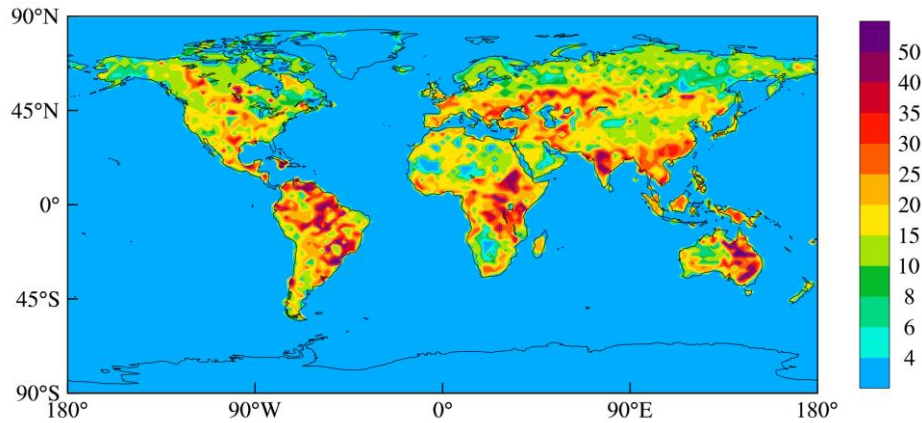
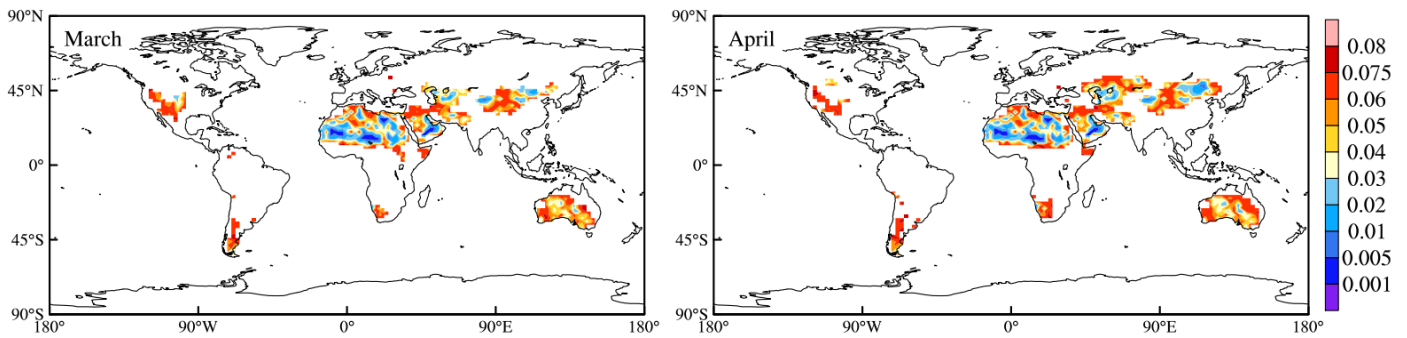


Fig 1. Schematic diagram and required input parameters in the dust emission scheme in GEOS-Chem.



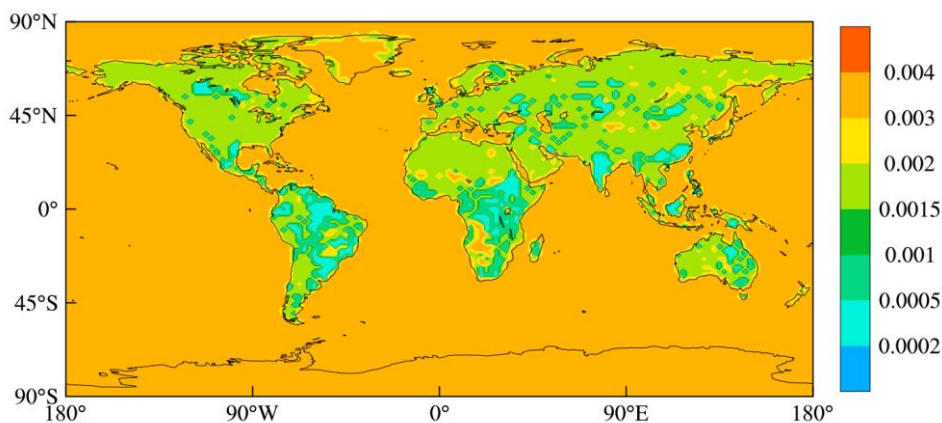
683

684 Fig 42. Updated input data of global  $M_{\text{clay}}$  (%). Data is derived from Shangguan et al. (2014) and is re-gridded to  $2^\circ$   
 685  $\times 2.5^\circ$  horizontal resolution in the model.



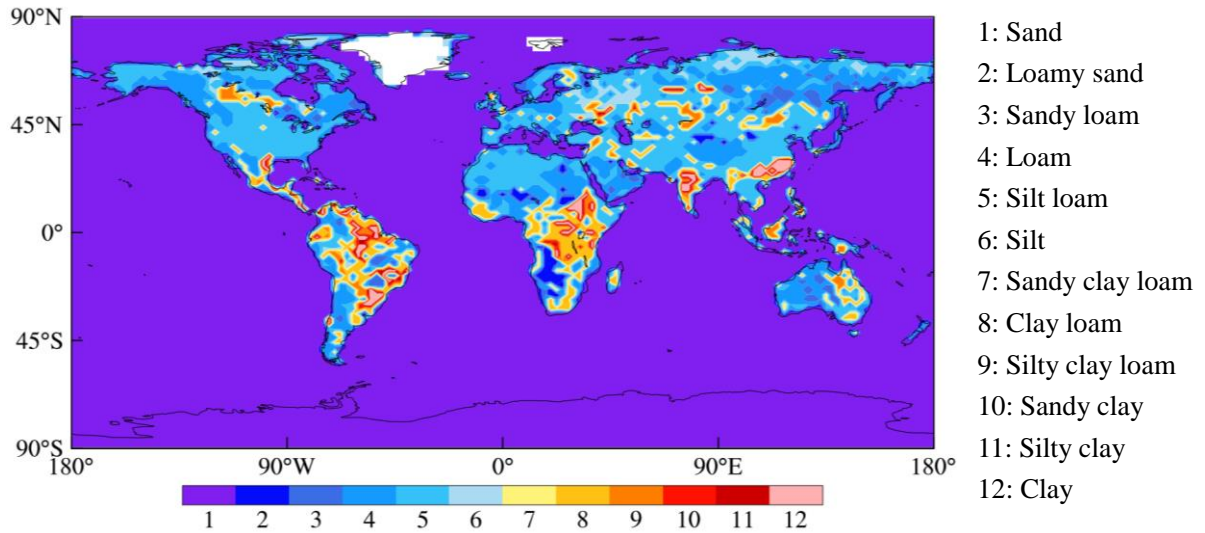
686

687 Fig 23. Monthly updated input data of global aerodynamic roughness length ( $Z_0$ ) (cm) in March (left) and April (right).  
 688 Data is derived from Prigent et al. (2005) and re-gridded to  $2^\circ \times 2.5^\circ$  horizontal resolution in the model.



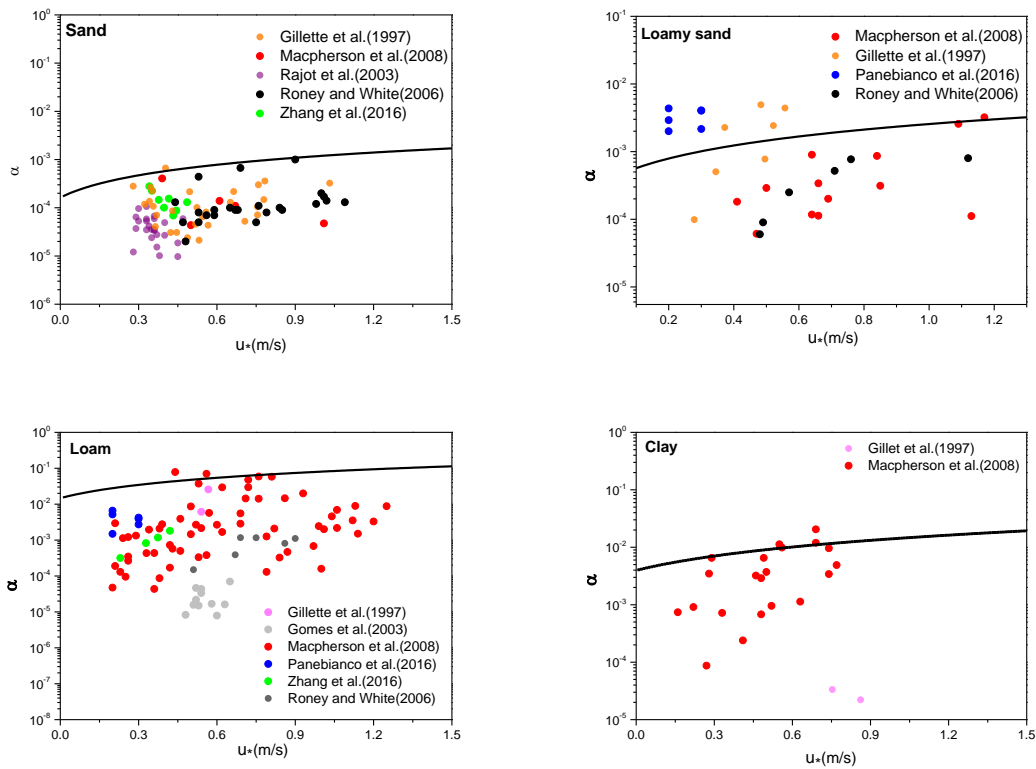
689

690 Fig 34. Updated global map of smooth roughness length ( $Z_{0s}$ ) (cm) estimated from the empirical relationship with  
 691 soil texture.



692  
693

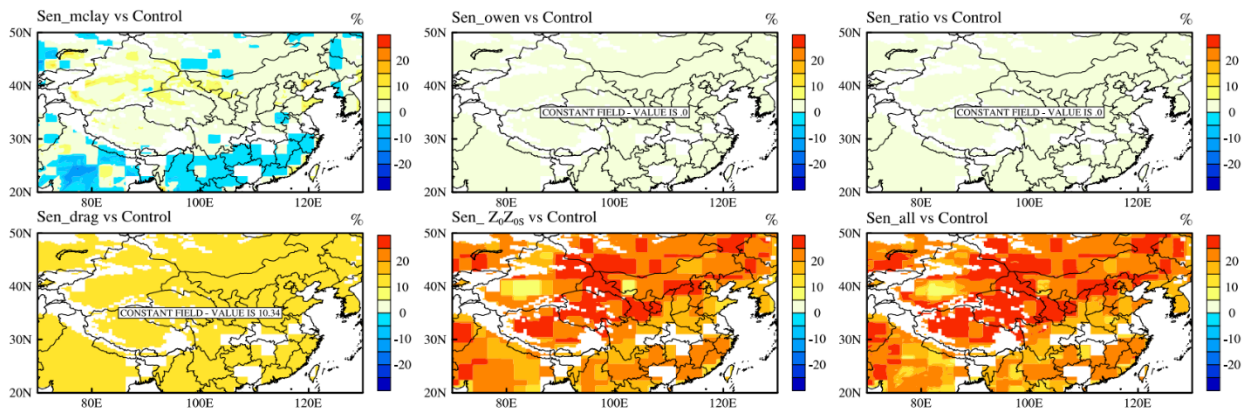
Fig 45. Global soil texture map based on the USDA classification.



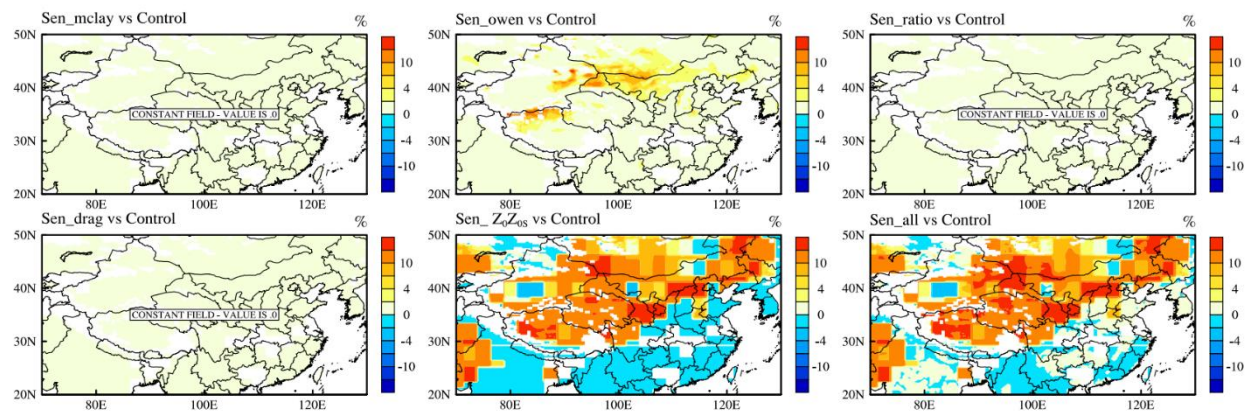
694  
695  
696

Fig 56. Updated sandblasting efficiency  $\alpha$  as a function of surface friction velocity  $u_*$  following Lu and Shao (1999) for sand, loamy loam, loam and clay and observations from the literature.

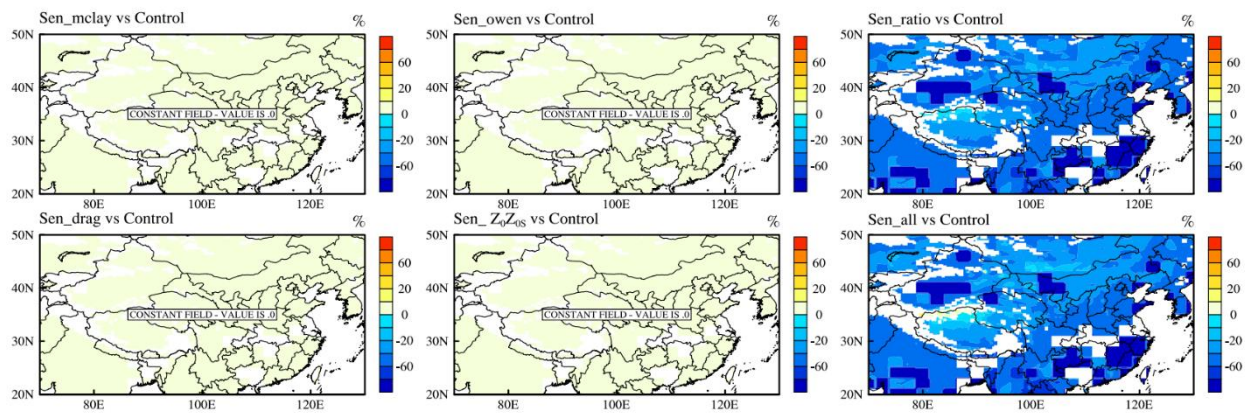
(a) Threshold friction velocity



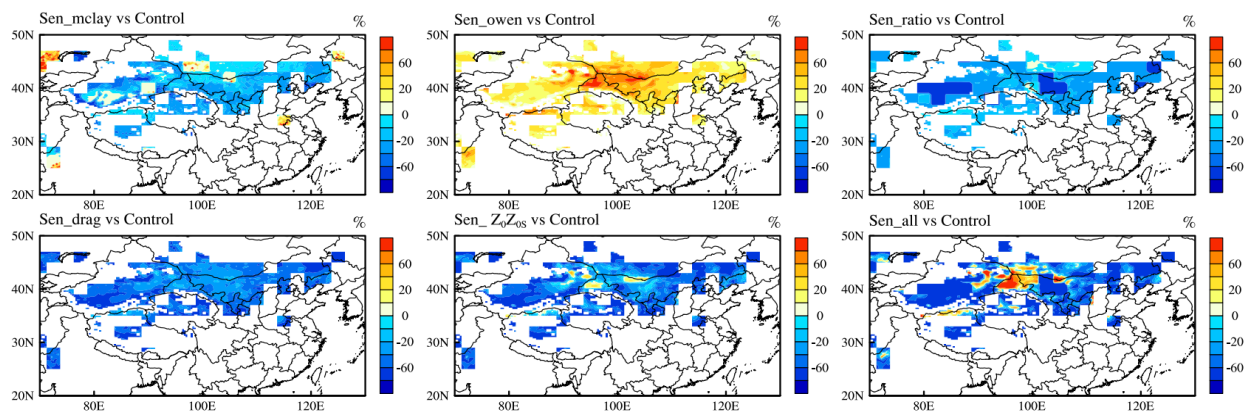
(b) Surface friction velocity



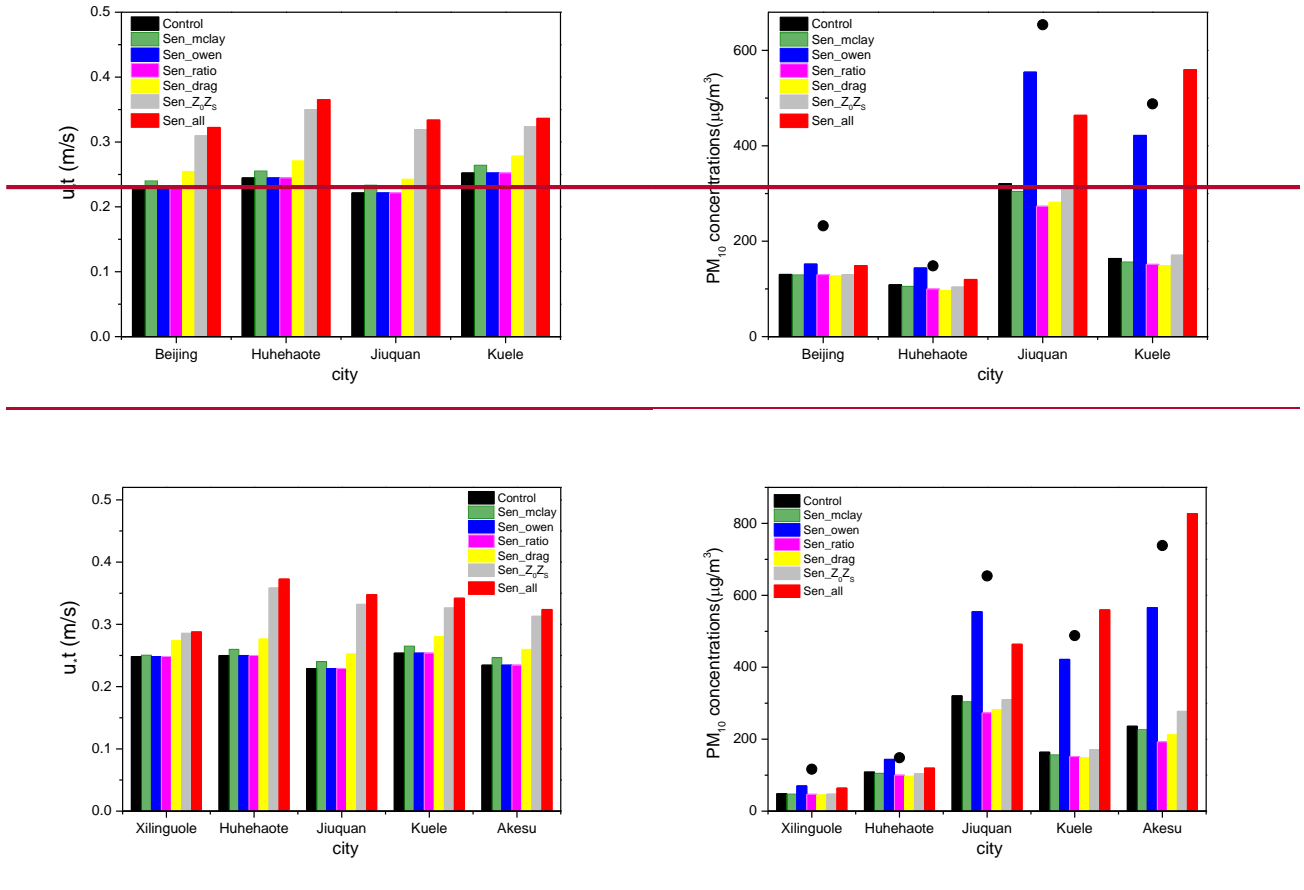
(c) Sandblasting efficiency



(d) Emission flux

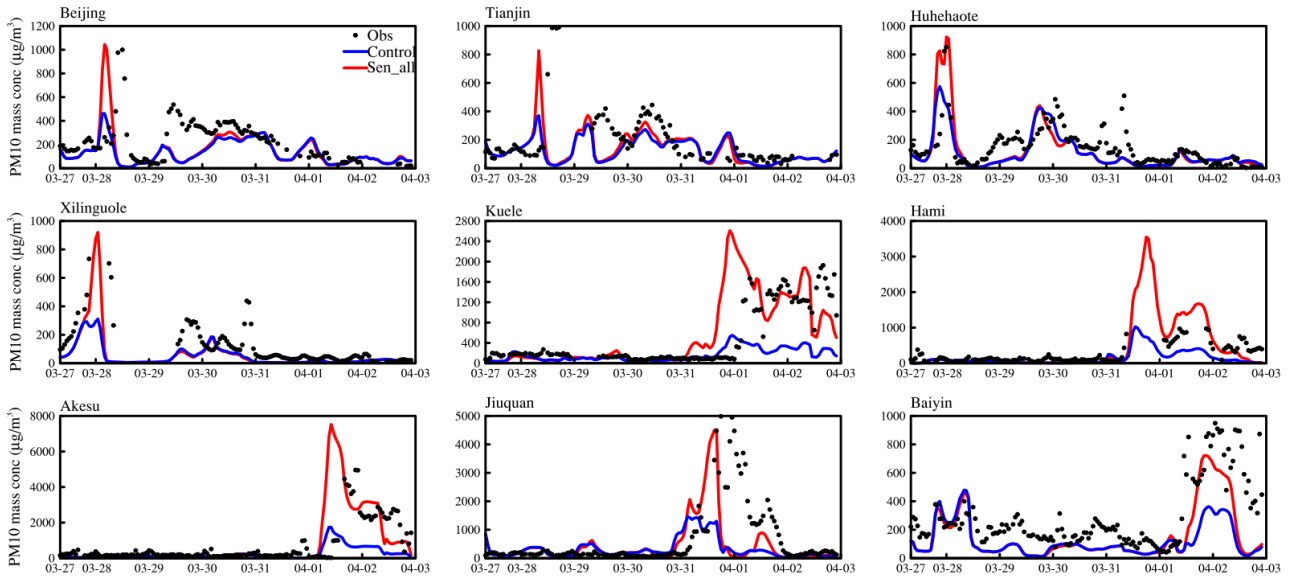


698 Fig 67. Relative difference (%) in simulated averaged threshold friction velocity  $u_{*t}$  (a), surface friction velocity  $u_*$   
 699 (b), sandblasting efficiency  $\alpha$  (c) and emission flux (d) between sensitivity simulations and control run during the  
 700 study period.

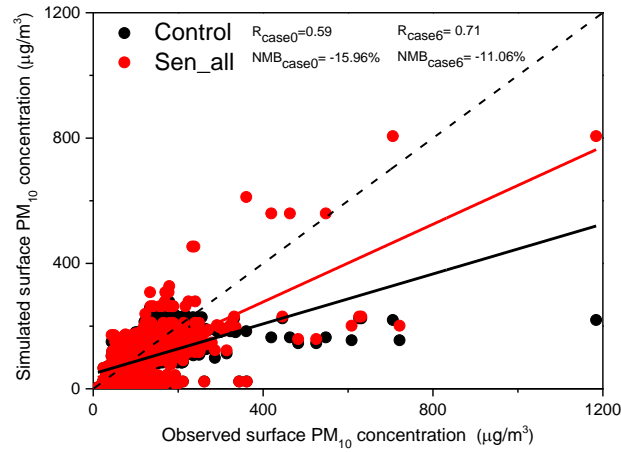


701 Fig 78. Comparisons of simulated averaged threshold friction velocity  $u_{*t}$  (left) and  $PM_{10}$  concentrations (right) at  
 702 selected sites. Black dots in right figure indicate the observed averaged  $PM_{10}$  concentrations.

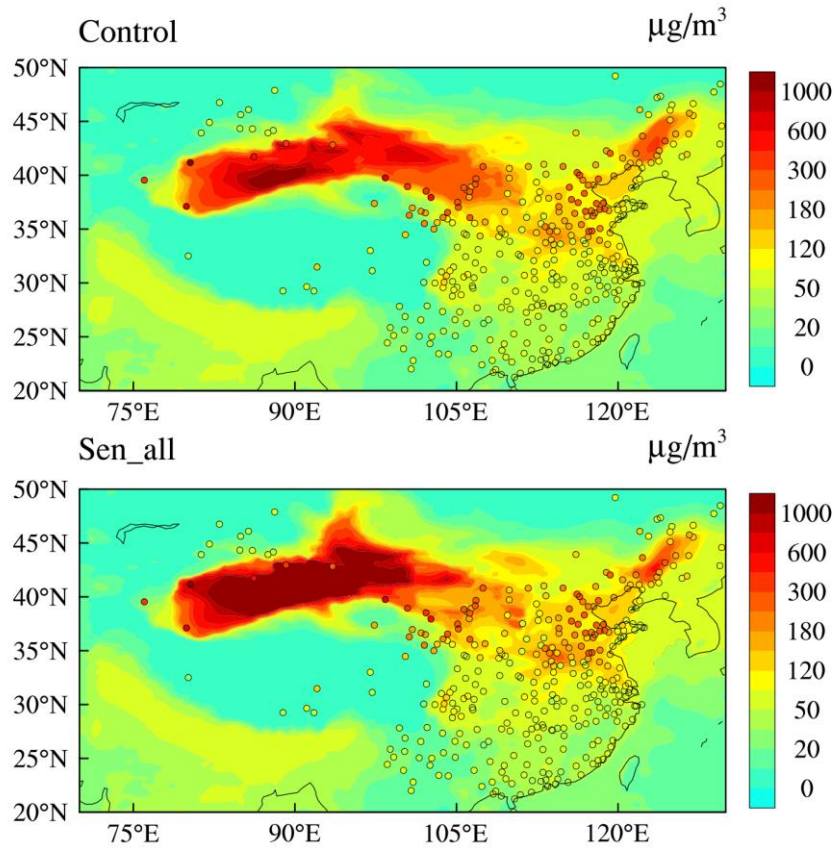




703 Fig 89. Temporal variation of hourly PM<sub>10</sub> concentrations from observations (black dots) and simulations of Control  
 704 run (blue line) and Sen\_all (red line) during the study period at nine selected sites.



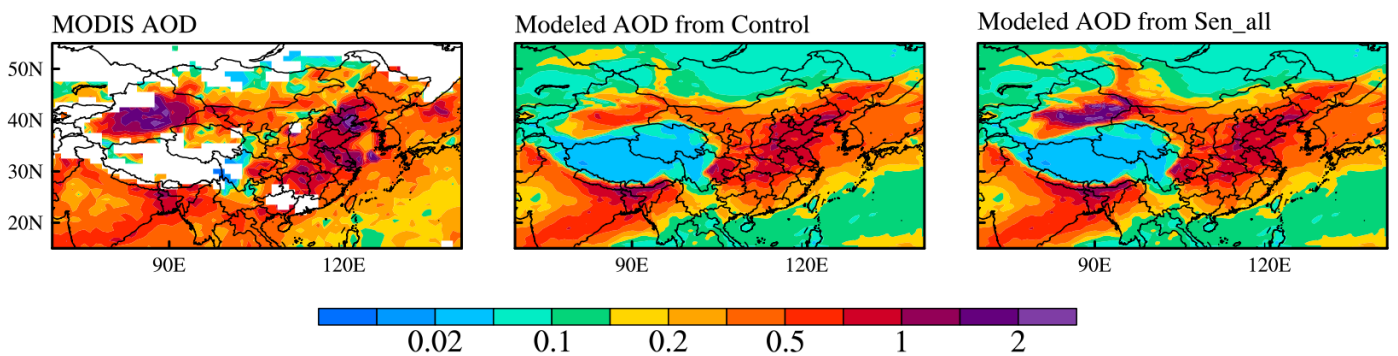
705 Fig 910. Comparison of modelled and measured surface PM<sub>10</sub> concentrations at observational sites. The dotted line  
 706 is the 1:1 line. Model results are taken from Control run and Sen\_all respectively.



707

708 Fig 4+11. Comparison of simulated averaged PM<sub>10</sub> surface concentrations from Control run (top) and Sen\_all (bottom)  
 709 with the observed values.

710



711

712 Fig 4+12. Spatial distribution of MODIS retrieved AOD at 550nm (left column) and simulated AOD at 550 nm from  
 713 Control run (middle column) and Sen\_all (right column). The simulation results are extracted at 13:00 local time to  
 714 match the MODIS observation time.